ngineering Center
n-Madison

METEOSAT II INTERFEROMETER SOUNDER: TRADEOFF STUDY

FINAL REPORT

A REPORT from the

Cooperative
Institute for
Meteorological
Satellite
Studies

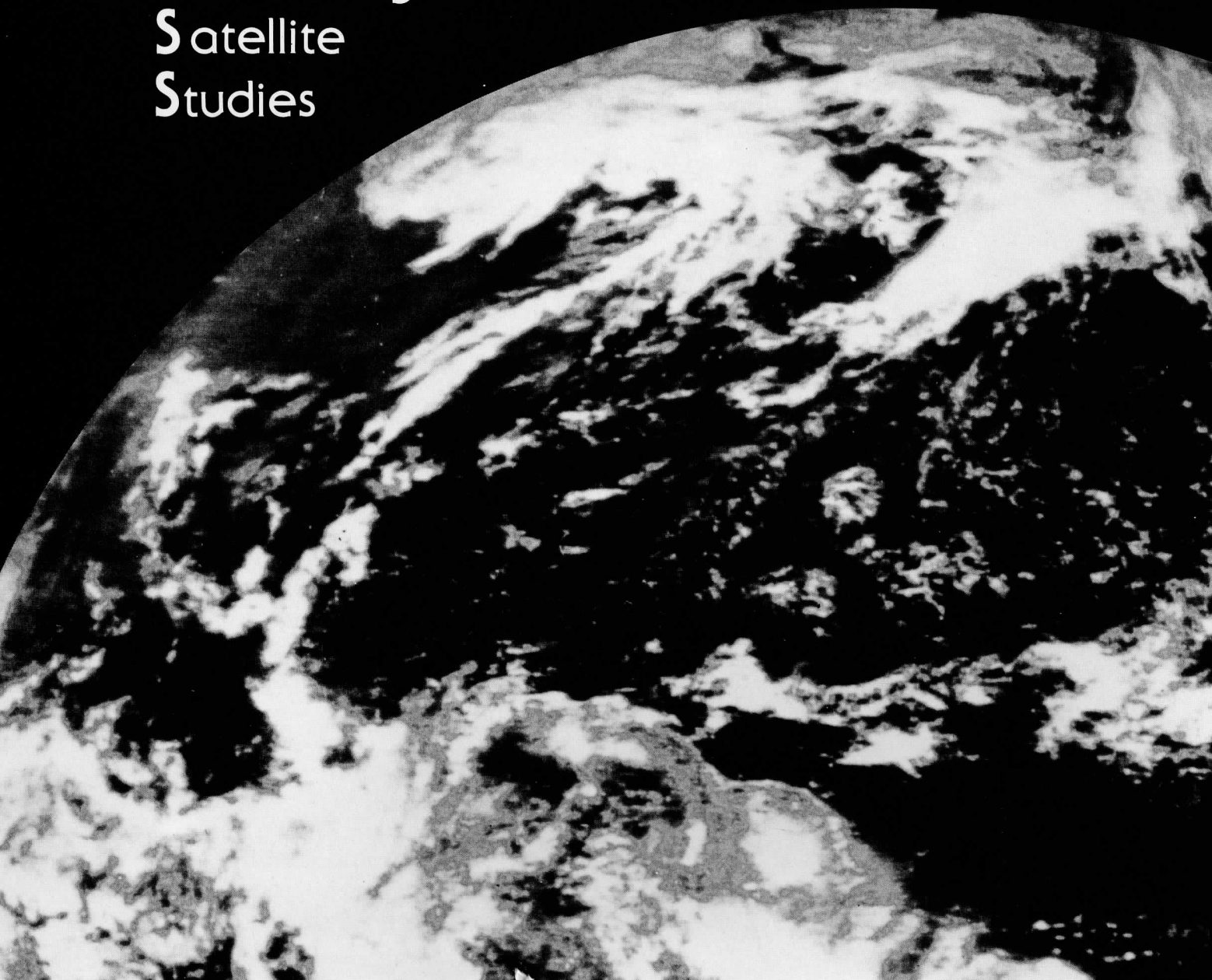

METEOSAT II INTERFEROMETER SOUNDER: TRADEOFF STUDY

FINAL REPORT

to

The European Organisation for the
Exploitation of Meteorological Satellites (EUMETSAT)

for fulfillment of

Contract #: EUM/CO/89/15

for the period of

1 July 1989 to 31 July 1990

submitted by

William L. Smith, Director

of

The Cooperative Institute for Meteorological Satellite Studies (CIMSS)

at the
University of Wisconsin-Madison
1225 West Dayton Street
Madison, Wisconsin 53706
608/263-4085

31 July, 1990

TABLE OF CONTENTS

1.0 Introduction

This is the final report of a tradeoff study for a Michelson interferometer sounder for the next generation Meteosat. The report provides a baseline instrument design for a geostationary temperature and water vapor sounder and shows its retrieval performance as a function of spectral resolution and instrument noise. The report also includes a tentative design for a low earth orbiting Michelson interferometer sounder for the purpose of comparison. Finally, some topics relevant to interferometer sounders in general are addressed. The design goal of the radiance measurements described in this report will permit operational temperature and water vapor retrieval accuracies approaching 1°C and 10%, respectively, with 1 km vertical resolution in the lower atmosphere.

An interferometer sounder in geostationary orbit is required to produce high vertical resolution temperature and moisture soundings as needed for:

(1) Defining atmospheric stability tendencies for forecasting local convection and associated weather.

(2) Providing one to three hourly interval sounding data input to regional mesoscale analysis/forecast models.

(3) Defining wind profiles for regional and global data assimilation systems through the animation of water vapor retrieved in eight narrow (1-2 km) vertical layers.

(4) Defining ocean and land surface skin temperature with high accuracy (~0.5°C) as needed for estimating surface heat fluxes.

(5) Providing the pressure heights of clouds with high accuracy (~25 mb), even for semi-transparent cirrus.

(6) Observing lower stratospheric and upper tropospheric ozone concentrations.

The Michelson interferometer is the most highly proven and mature technology for providing continuous spectra of earth-atmosphere radiance with relatively high spectral resolution. Simulations and experimental data from high altitude aircraft with the High-resolution Interferometer Sounder (HIS) have demonstrated that soundings of atmospheric temperature and water vapor can be achieved with vertical resolutions and accuracies two to three times better than that currently achievable with filter radiometer instruments (Appendix B). This improvement is crucial for achieving the sounding accuracy needed to resolve stability features responsible for localized weather and for satellite soundings to be useful in numerical weather analysis/forecast models. Also, the relatively high spectral resolution of the radiometric data permits surface skin

temperature and cloud pressure altitudes to be defined with much higher accuracies than are achievable with current sounding/imaging radiometers.

The unique advantage of implementing an interferometer sounder on a geostationary satellite is that both the local time tendency and the mass motion of the atmosphere can be observed. The tendency observation is important for local forecasting. The moisture motion observation, of as many as eight distinct tropospheric layers, provides wind soundings useful for input to global as well as regional data assimilation systems. Also, the use of the geostationary satellite optimizes the capability for observing the important near-surface temperature, water vapor, and ozone features. This optimization occurs because one is able to observe at times when cloud obscuration is a minimum and when the surface background temperature possesses the greatest contrast with the overlying atmosphere.

The higher information content provided by the quasi-continuous spectral measurements of outgoing radiance is extracted from a correspondingly larger number of spectral channels. Fortunately, a new very efficient retrieval method for the simultaneous retrieval of the desired parameters has been developed to enable the processing to be accomplished at real-time rates even with today's medium-class computers. Tests of this highly efficient retrieval algorithm have been conducted with experimental aircraft data to demonstrate the achievement of the accuracy desired.

This report defines a conservative baseline specification for the next generation Meteosat. It is conservative in that all the requirements can be achieved with currently available hardware and the data can be handled with today's mid-class computers. The spectral and spatial resolutions are appropriate for achieving the desired meteorological products and accuracies at low risk to cost and performance. This report provides performance comparisons of the baseline interferometer system with a filter radiometer. The weight, power, and size requirements of the baseline Meteosat interferometer is comparable to that of a filter radiometer, even though the sounding performance is greatly improved.

2.0 Assumptions and Objectives

The initial assumptions and tradeoff considerations for this study are based on the fundamental scientific objective of performing enhanced temperature and water vapor soundings for the European area. In addition, a requirement for a full disk capability has been assumed. Figure 1 emphasizes the desire for sounding the full earth disk (A) as well as the European sector (B). Other important scientific possibilities, such as vertical wind profiling via water vapor tracking within narrow vertical layers and ozone retrieval, are assumed, but the design has not

been optimized for those quantities. It has been assumed that the sounder would be a part of a three axis stabilized satellite with a clear view of the full earth disk, a view to deep space off the limb of the earth, and with access to the celestial north or south pole for passive radiative cooling.

An important practical objective is to make the instrument as simple, reliable, and inexpensive as possible, but at the same time maintain in-orbit operational flexibility. Therefore, options which might provide substantial simplifications are sought for evaluation, in addition to performance enhancement options.

The general approach of this study is to define a baseline instrument from which options for operational and design variances can be evaluated using simulations of sounding performance. Temperature and water vapor sounding simulations will use the simultaneous retrieval technique developed for HIS aircraft data (See Appendix B).

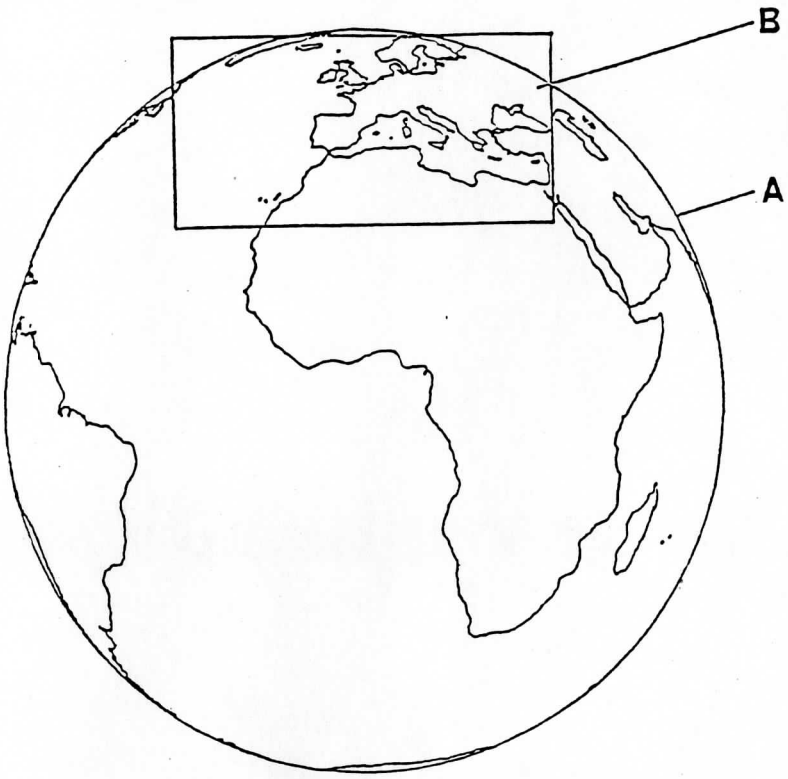

Figure 1. Meteosat II sounder full disk capability (A) and the European sector (B).

The specific design objective is to obtain radiance measurements which will permit operational temperature and water vapor retrieval accuracies approaching 1°C and 10%, respectively, with 1 km vertical resolution in the lower atmosphere.

3.0 Topics of Interest

The main body of this report is divided into topics of interest for sounding with a Michelson interferometer. Topics include a discussion of 1) the geostationary sounder baseline definition, 2) the geostationary sounder retrieval simulations, 3) the geostationary interferometer sounder compared to an interferometer for a low orbiter design, 4) interferometric calibration issues, 5) the impact of scene variations, 6) interferometer noise specifications, and 7) sounder data compression techniques.

3.1 Geostationary Sounder Baseline

The baseline design for the Meteosat II sounder was developed in consultation with the Santa Barbara Research Center (SBRC), a subsidiary of Hughes Aircraft Company. The geostationary sounder design is the latest in a series of such designs developed jointly by the University of Wisconsin and SBRC dating back to 1981. The Meteosat II baseline design is considered optimal for temperature and water vapor sounding using proven detector technology and passive radiative cooling. The principal driver for the geostationary design is the telescope diameter, which must be large enough to obtain good signal to noise but not so large that the instrument volume and mass become unacceptably large. The choice of 40 cm for the telescope diameter is a compromise which increases the photon collecting capability over the current GOES design (30 cm diameter) while keeping the mass and volume within an overall envelope of 150 kg and about 1 m^3. An important distinction from GOES-I (and the CIMSS/SBRC GOES-MOD design) is that the Meteosat II sounder telescope uses an off-axis paraboliod which makes the design less susceptible to thermal distortion of the imaging optics.

This section includes the following subtopics; hardware definition, radiometric performance, and operating modes.

3.11 Hardware Definition

A schematic of the optical layout of the geostationary interferometer sounder is shown in Figure 2. The baseline design for the geostationary infrared sounder is a single Michelson interferometer with continuous and complete optical path difference (OPD) scanning. The maximum optical path length is assumed to be programmable up to some mechanical limit. This allows the operational flexibility of choosing among local area coverage at high vertical resolution, regional area coverage at medium resolution, and global coverage at a somewhat lower vertical resolution. Table 1 gives the characteristics of the baseline design for the Meteosat II sounder used in this report. Adequate noise performance over a wide region (3.7 - 15 microns) of the

infrared emission spectrum is achieved by dividing the spectral coverage in three broad spectral bands. The spectral coverage includes the 15μm CO_2 temperature sounding region, the 8μm window, the 9μm ozone band, the 10μm window, the 12μm H_2O band, the 5μm carbon monoxide band, the 4μm N_2O/CO_2 sounding region, and the 3μm window. The earth scan mirror uses a step and settle raster scan design. In addition, the design makes use of array detectors (3x3 cluster) to give parallel spatial sampling, thus increasing the spatial coverage rate by a factor of nine over a single field of view (FOV) instrument.

The interferometer uses a constant velocity continuous motion Michelson mirror. The interferogram is laser sampled using a solid state laser which provides a high degree of wavelength integrity. The design uses a passive radiative cooler, which requires a clear view to space.

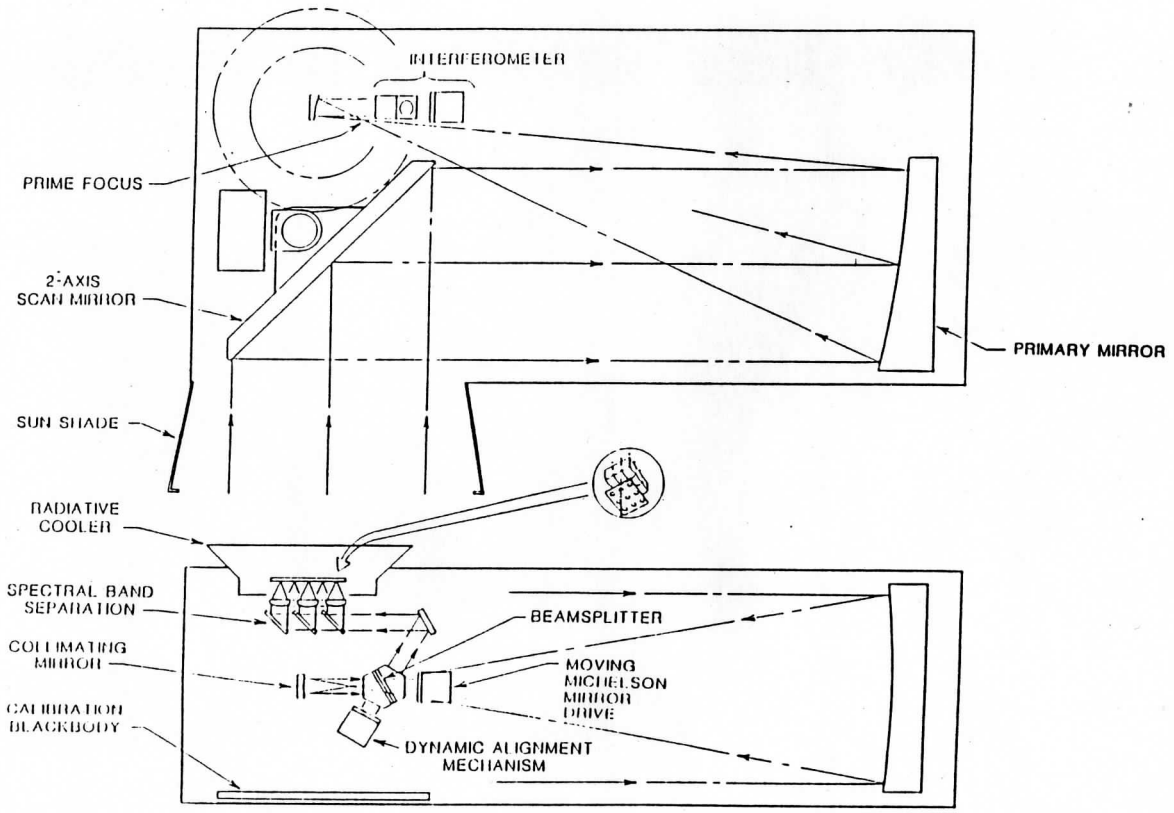

Figure 2. Meteosat II sounder optical layout showing the off-axis telescope design which avoids thermal distortion of the imaging optics. Courtesy of SBRC.

Table 1. Characteristics of the METEOSAT Instrument Design

Spectral range and Maximum Resolution (cm^{-1})	
Band 1 ($\Delta\nu = 0.33\ cm^{-1}$)	600-1100
Band 2 ($\Delta\nu = 0.33\ cm^{-1}$)	1100-1800
Band 3 ($\Delta\nu = 0.33\ cm^{-1}$)	2000-2700
Field of view (FOV)	
Simultaneous array pattern	3 x 3
Single FOV (side of square)	10 km, 280 μr
Center-to-center spacing	16.6 km, 465 μr
Telescope/Collimator	
Telescope type	Off-axis paraboloid
Telescope diameter	40 cm
Telescope f/#	f/1.1
Telescope/collimator afocal ratio	10
Area-solid angle product/FOV	$9.92 \times 10^{-5}\ cm^2$-sr
Interferometer	
Type:	Auto-aligned Plane mirror Michelson
Mirror Scan length and rate	Programmable
Max. mirror scan length	±0.75 cm (±1.5 cm OPD)
Mirror scan rate	1.55 cm/s (3.1 cm OPD/sec)
Laser	1.06μm diode pumped Nd:YAG
Beamsplitter:	
Substrate	KCl
Coatings (1/4 λ at 3.3 μm)	Ge + Sb_2S_3
Beam diameter	4 cm
FOV (Max. dimension of array)	17 mr
Detectors	
Type	
Band 1	PC HgCdTe
Bands 2 & 3	PV HgCdTe
Size (side of square)	
Band 1	0.0082 cm
Bands 2 & 3	0.0101 cm
Temperatures	
Telescope	290 K
Interferometer	200 K
Detectors	85 K

3.12 Radiometric Performance

For an interferometer with constant OPD mirror velocity the relationship for apodized detector noise [one component of spectral noise (NEdT)] is

$$NEN = \frac{\sqrt{[A_d]} \cdot X \cdot 10^7}{A_0 \cdot \Omega \cdot t_0 \cdot D^* \cdot \sqrt{[1/(2\ T_i)]}} \quad [\frac{mW}{m^2\ sr\ cm^{-1}}] \qquad (1)$$

where,

A_d = The area of the detector [cm^2]
X = Maximum optical path difference [cm]
A_0 = The area of the optics aperture [cm^2]
t_0 = The overall optical transmission.
Ω = The optics solid angle [sr]
T_i = The integration time per scene [sec]
D^* = Detector spectral response [cm√Hz/W]

The noise has been optimized at the long wavelength end of each band. The band edges have been selected to optimize the science return relative to this noise performance. The expected noise performance is given in Table 2 and is shown graphically in Figure 3. These noise levels should be compared to the figures in section 3.23 on retrieval performance versus spectral noise. See also section 3.6 for a discussion of the specification of noise for an interferometer sounder.

Table 2. Expected noise performance (apodized) for METEOSAT II sounder.

Band Name	**Band 1**	**Band 2**	**Band 3**
Minimum ν, cm^{-1}	600	1100	2000
Maximum ν, cm^{-1}	1100	1800	2700
NEN, $mW/m^2sr\ cm^{-1}$			
@ Minimum ν	0.18	0.042	0.0060
@ Mid-band	0.26	0.056	0.0070
@ Maximum ν	0.33	0.069	0.0081
NEΔT, °C *			
@ Minimum ν	0.14	0.05	0.05
@ Mid-band	0.21	0.15	0.19
@ Maximum ν	0.39	0.55	0.74
Maximum OPD (cm)	1.5	1.5	1.5
Maximum Dwell Time (s)	1.0	1.0	1.0
Transmission, τ	0.14	0.14	0.14
D*peak, cm√Hz/W	3.5+10	1.9+11	1.3+12

* Bands 1 and 2 @ 260 K. Band 3 @ 280 K.

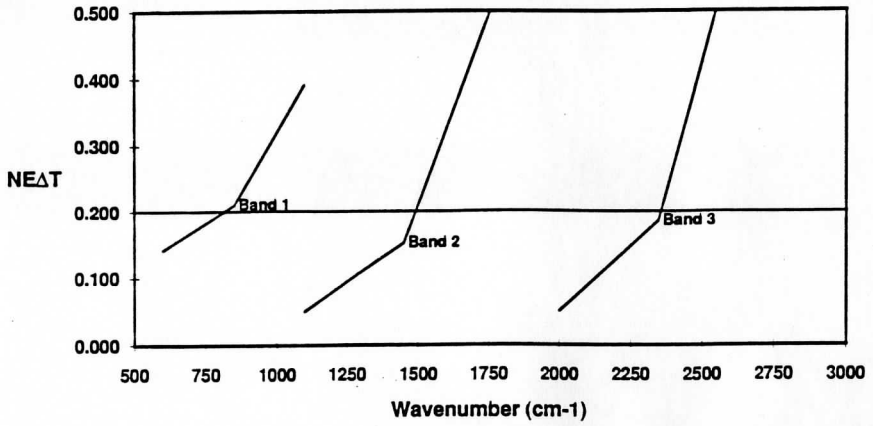

Figure 3. Meteosat II sounder noise performance in high resolution mode expressed as noise equivalent brightness temperature (NEdT). The performance meets a specification of 0.2 K in NEdT at 260K (280K in Band 3), in an average sense over the bands. See also section 3.6.

3.13 Operating Modes

The baseline instrument, as conceived, has considerable in-orbit operational flexibility. The earth scan system can provide a raster scan (i.e. a sequence of rows within a rectangular area) for arbitrary rectangular regions up to a full disk image. It has three spectral resolution modes with minimum dwell time in each mode of 0.1 sec (low), 0.5 sec (medium), and 1.0 sec (high). Spectral mode definitions are given in Table 3.

Table 3. Meteosat II Sounder Spectral Resolution Mode Definitions

MODE	Max. OPD	Resolution Element	Dwell Time
HIGH	±1.5 cm	0.33 cm^{-1}	1.0 sec
MEDIUM	±0.75 cm	0.66 cm^{-1}	0.5 sec
LOW	±0.15 cm	3.30 cm^{-1}	0.1 sec

Resolution Element (unapodized) = $1/(2 \cdot X_{max})$

The sounder has nine fields of view in a 50x50 km array, where each field of view diameter is 10 km at nadir spaced 16.6 km apart. The amount of time necessary to cover a rectangular area is equal to the product of the number of steps of the cluster array multiplied by the time spent dwelling in each location. For example, in low resolution mode (0.1 sec dwell) a 12,000 x 12,000 km area encompassing the earth disk could be covered in $(12{,}000/50)^2 \cdot 0.1$ sec = 5760 sec, i.e. 96 minutes. In an example of regional sounding in high resolution mode (1.0 sec dwell), a 3000 x 3000 sounding region could be covered in one hour obtaining high vertical resolution soundings at 16.6

4 gives a few examples of possible coverage times. In order to further reduce area coverage times one can make use of the step and dwell capability of the sounder telescope to sample 50 x 50 km subregions at intervals larger than 50 km. Table 4 gives an example of regional and global area coverage times using 50 km clusters spaced 100 and 150 km apart. The ability to select rectangular sounding regions of arbitrary size, and to choose among the possible vertical resolution modes and spatial sampling strategies gives the Meteosat sounder the operational flexibility needed to meet the changing needs of the meteorological operating environment.

Table 4. METEOSAT II Sounder Coverage Times

CLUSTER SEPARATION		SPECTRAL MODE High (1 sec)	Medium (0.5 sec)	Low (0.1 sec)
50 km	**Regional**	**60 min**	**30 min**	**6 min**
	Global	*16 hrs*	*8 hrs*	*96 min*
100 km	**Regional**	**15 min**	**7.5 min**	**1.5 min**
	Global	*4 hrs*	*2 hrs*	*24 min*
150 km	**Regional**	**6.7 min**	**3.3 min**	**40 sec**
	Global	*1.8 hrs*	*0.9 hrs*	*11 min*

Spatial Resolution is 10 km at nadir with a 16.6 km separation within each 3x3 FOV cluster
[Regional = 3000 x 3000 km] *[Global = 12000 x 12000 km]*

3.2 Geostationary Sounder Retrieval Capability

In this section, the dependence of temperature and water vapor retrieval error on spectral resolution and spectral noise will be explored. The principal conclusions are contained in Figures 4a-c for temperature, water vapor, and vertical resolution respectively. The curves show both the advantage of the interferometer design over that of a filter radiometer and the ability of the interferometer to achieve the sounding performance required to have a positive impact on forecast models.

3.21 Baseline Sounding Enhancement

The Meteosat II sounder is intended to enhance the sounding capabilities beyond the current generation of geostationary radiometer sounder, which uses a filter wheel to sequentially measure a small number of relatively broad spectral channels (10s of wavenumbers). In contrast, the interferometer sounder has a much larger number of channels (over 4000 in high resolution mode) each with a much narrower spectral resolution element (as small as 0.33 cm^{-1}). The

mode) each with a much narrower spectral resolution element (as small as 0.33 cm^{-1}). The remainder of this section shows the dramatic improvement in sounding vertical resolution and retrieval uncertainty that results from these enhanced measurements.

Figure 4a shows the root-mean-square (rms) temperature retrieval error at standard "mandatory" pressure levels obtainable with the GOES-I filter radiometer compared with the temperature retrieval error expected from the baseline Meteosat II interferometer sounder discussed in section 3.1. Similarly, Fig. 4b shows the fractional error of retrieved precipitable water. The curve labeled "GLOBAL" corresponds to the baseline interferometer low spectral resolution mode (3-4cm^{-1}) which has the same dwell time as the filter radiometer and hence similar area coverage capabilities. The curve labeled "MESOSCALE" corresponds to the interferometer sounder high spectral resolution mode.

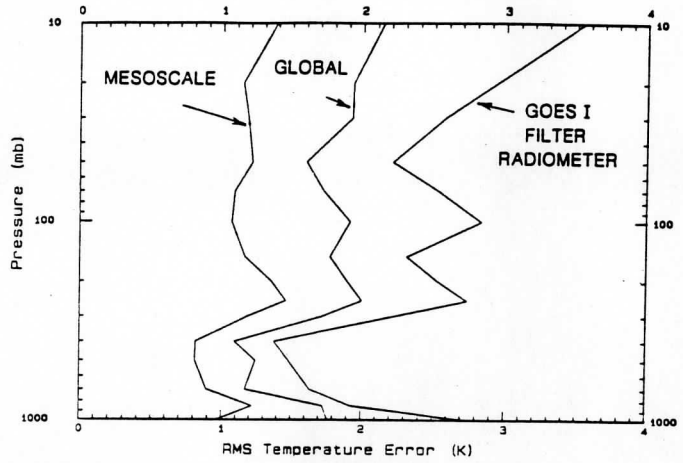

Figure 4a. RMS Temperature Retrieval Error

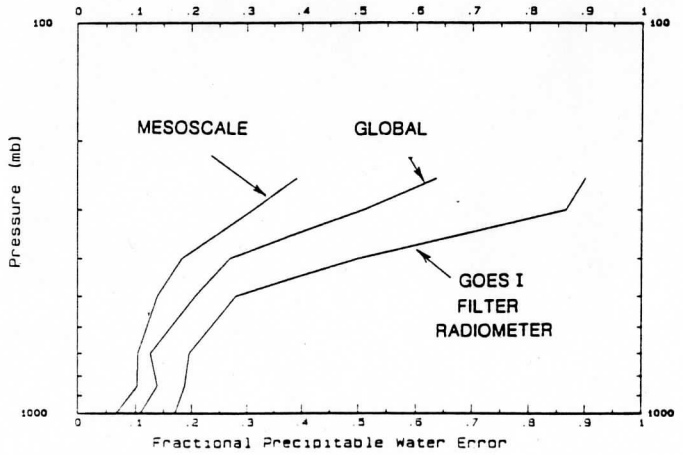

Figure 4b. RMS Precipitable Water Retrieval Error

Fig. 4c shows the vertical resolution of temperature, using the concept of Backus and Gilbert, 1970, and Rogers, 1986, for the same instruments. The dramatic improvement of the low spectral resolution interferometric data over that of the filter radiometer is evidence of the importance of the continuous nature of the spectra obtained naturally with the interferometer. The improvement in sounding accuracy obtainable from the same baseline instrument when operated in high spectral resolution mode shows the additional benefit of resolving the carbon dioxide and water vapor line structure in the infrared emission spectrum. This mode is best suited for the study of the precursors to local severe weather both because of the high vertical resolution provided and because the additional dwell time required in this mode reduces the area coverage rate.

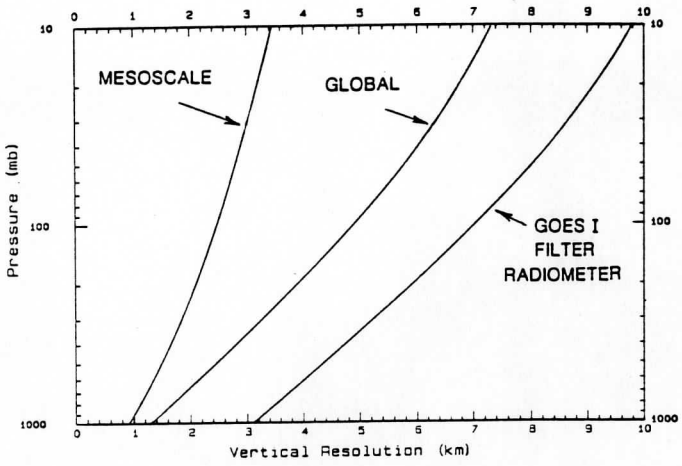

Figure 4c. Vertical Resolution of Temperature

3.22 Spectral Resolution Tradeoff

One of the important tradeoffs in infrared temperature sounding from space is retrieval performance versus spectral resolution. Figures 5a-c demonstrate this relationship for temperature, water vapor, and vertical resolution by showing the simulated retrieval performance for each of the baseline spectral resolution modes. "HIGH" refers to high resolution mode, "MEDIUM" refers to medium resolution mode, and "LOW" refers to low resolution mode. See Table 3 for mode definitions. Figures 5a-c are a comparison of retrieval performance assuming the same spectral noise, NEdT, for each resolution. Under this assumption, the benefit of higher spectral resolution is clear. With higher spectral resolution there are more channels of data in each spectral band useable for noise reduction and the individual channels are "clearer", that is

there is less smearing of line centers into line wings and hence improved ability to discriminate upper level from lower level radiative contributions. For instance, Fig. 5c shows that, with a spectral noise of 0.25°C, the high resolution mode has a vertical resolution of about 1.2 km at the 800mb level whereas in low resolution mode the vertical resolution has degraded to 1.8 km. The medium resolution mode is intermediate between the two. While this analysis is correct for equal noise, in fact, in normal operation the three operating modes will likely each have different noise levels associated with them. This leads us to an analysis of the dependence of the retrieval on spectral noise.

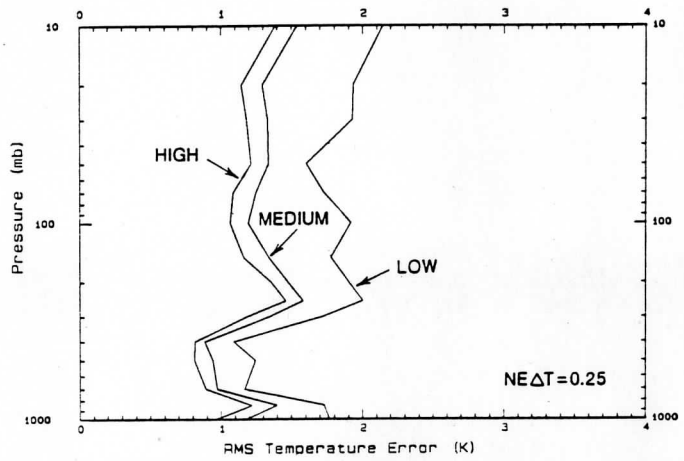

Figure 5a. RMS Temperature Retrieval Error vs Spectral Resolution

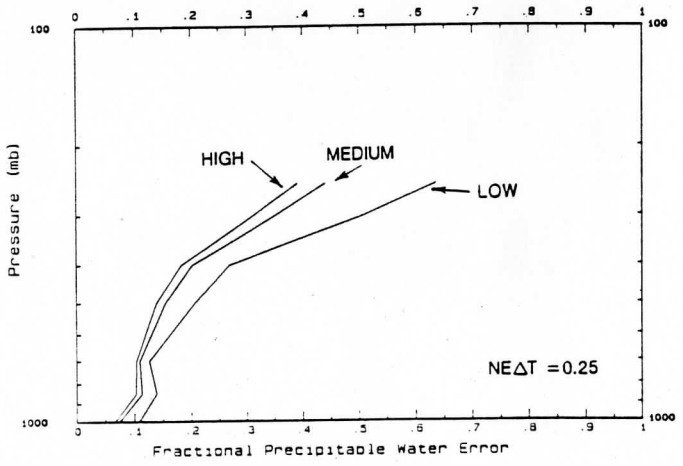

Figure 5b. RMS Precipitable Water Retrieval Error vs Spectral Resolution

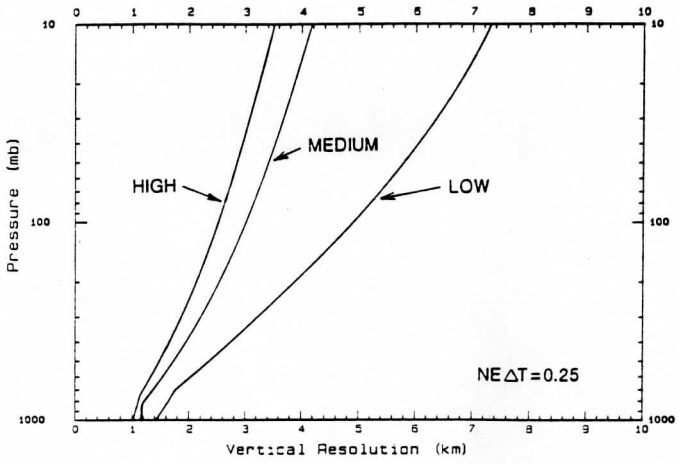

Figure 5c. Temperature Vertical Resolution vs Spectral Resolution

3.23 Spectral Noise Tradeoff

Another tradeoff in the instrument design important to retrieval performance is the dependence of retrieval accuracy on spectral noise. Figures 6a-c show, with medium resolution as an example, the dependence of varying spectral noise (NEdT) on the retrieval of temperature, water vapor and vertical resolution. As shown in Fig. 6a, a reduction of the spectral noise (NEdT) causes a steady improvement in the retrieval accuracy (e.g. reduction of NEdT from 1.0°C to 0.125°C at the 700mb level reduces the rms temperature retrieval error from 1.3°C to 0.8°C in medium resolution mode). The same improvement is evident in precipitable water retrieval, Fig. 6b, and in vertical resolution, Fig. 6c.

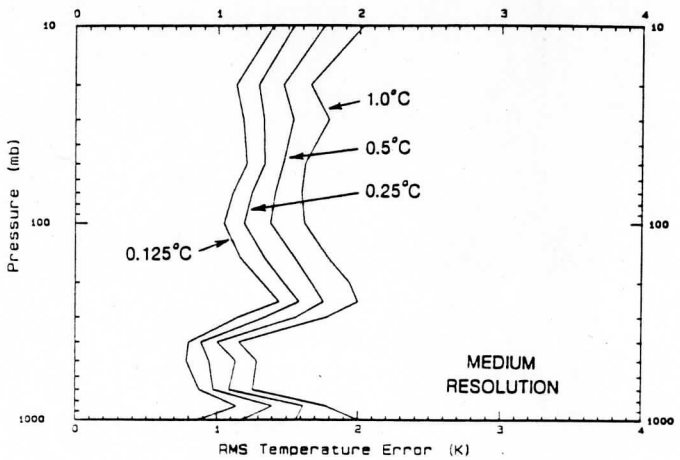

Figure 6a. RMS Temperature Retrieval Error vs Spectral Noise

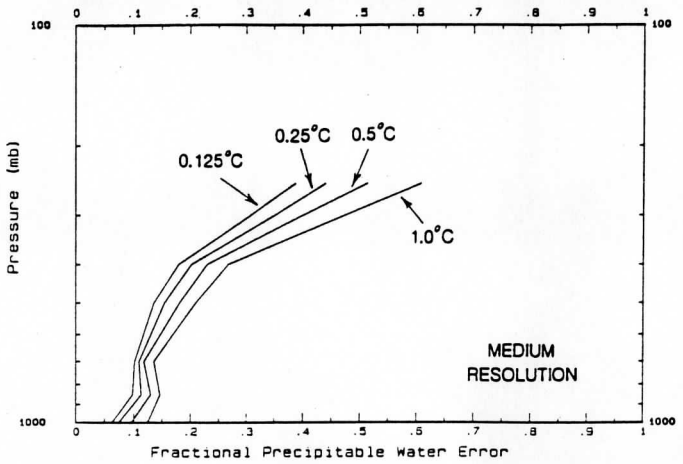

Figure 6b. RMS Precipitable Water Retrieval Error vs Spectral Noise

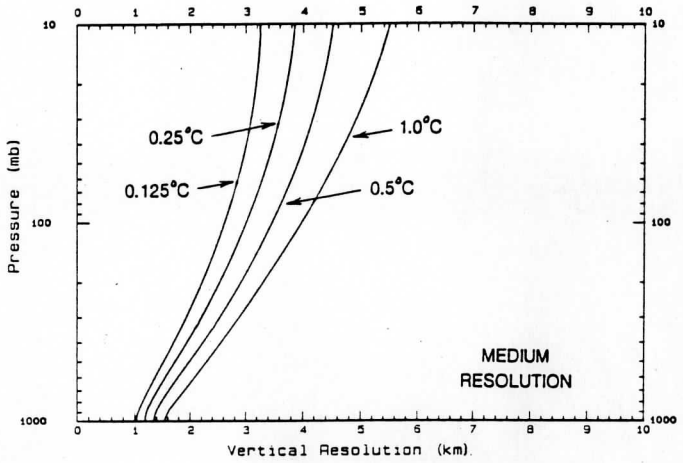

Figure 6c. Temperature Vertical Resolution vs Spectral Noise

Curves such as these have been used to estimate the noise level to which instrument performance should be designed. The baseline design radiometric performance given in section 3.12 has an average spectral noise level of about 0.2°C in each band (as shown in Figure 3 for high resolution mode). The dependence of vertical resolution and retrieval error on spectral noise is similar for high, medium, and low resolution modes. However, since each resolution mode has a different associated integration time, a direct comparison of the simulation performance of each spectral resolution should be considered with the same sounding dwell times in each mode. In this case, sounding dwell time is defined to be the total time the earth scan mirror spends in a given location, perhaps making repeated measurements to improve the signal to noise of the measurement. Such a comparison has been performed and the results are given in Appendix A. The main conclusions of this analysis are that; (1) a low resolution interferometer has a substantial advantage over a filter wheel radiometer with similar area coverage capabilities, (2) given the same sounding dwell times, both the medium and high resolution modes have a significant

performance improvement over that of low resolution mode, and (3) the high resolution mode always provides the best vertical resolving capability.

The Meteosat II sounder baseline design presented here is an attractive instrument for achieving the desired sounding performance while maintaining the spatial coverage capabilities of existing systems through its low resolution mode.

3.3 Polar Orbiting Interferometer Thermal Sounder (ITS)

The performance of the geostationary interferometer sounder presented in the previous section is compared in this section to a low earth orbiting instrument, referred to here as the Interferometer Thermal Sounder (ITS). This tentative ITS baseline design was developed jointly by the Santa Barbara Research Center (a subsidiary of Hughes Aircraft Company) and the University of Wisconsin.

3.31 ITS Baseline Definition

A diagram of a feasible low earth orbiting interferometer sounder is shown in Figure 7. The instrument characteristics are presented in Table 5. This ITS conceptual design has the telescope(s) behind the interferometer. The four telescopes shown in Figure 7 are only illustrative. The actual number will match the number of spectral bands in the design plus a possible higher resolution option obtained using an optical path offset.

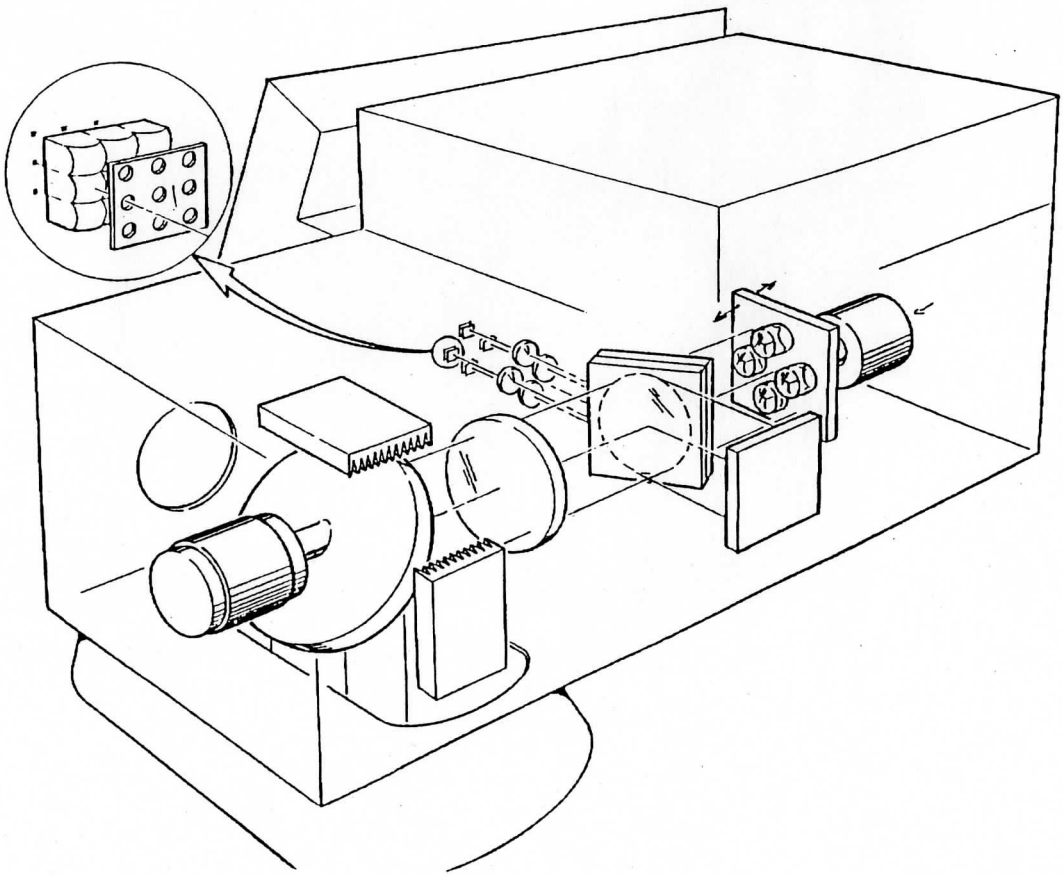

Figure 7. Low earth orbiting Interferometer Thermal Sounder (ITS). Courtesy of SBRC.

Table 5. Characteristics of the ITS Instrument Design

Spectral range and Resolution (cm^{-1})*	
Band 1 ($\Delta\nu = 0.5\ cm^{-1}$)	620-1150
Band 2 ($\Delta\nu = 0.5\ cm^{-1}$)	1210-1740
Band 3 ($\Delta\nu = 0.5\ cm^{-1}$)	2150-2720
Field of view (FOV)	
Simultaneous array pattern	3 x 3
Single FOV diameter	10 km, 12 mr
Center-to-center spacing	20 km, 24 mr
Telescopes	
Number	3 or 4
Telescope type	Single lens
Telescope diameter	2.54 cm
Area-solid angle product/FOV	$5.6 \times 10^{-4}\ cm^2$-sr
Interferometer	
Type:	Michelson 2-port Corner Mirror
Mirror scan length	±0.5 cm (±1.0 cm OPD)
Mirror scan rate	5.0 cm/s (10 cm OPD/sec)
Laser	1.06μm diode pumped Nd:YAG
Beamsplitter:	
Substrate	KCl
Coatings (1/4 λ at 3.3 μm)	Ge + Sb_2S_3
Beam diameter	8 cm
Detectors	
Type	
Band 1	PC HgCdTe
Bands 2 & 3	PV HgCdTe
Size (side of square)	0.020 cm
Temperatures	
Telescope	290 K
Interferometer	200 K
Detectors	85 K

*Spectral Resolution (unapodized) = 1/(2 · Maximum Optical Path Difference)

The spectral coverage is divided into bands to improve noise performance and includes the 15μm CO_2 temperature sounding region, the 8μm window, the 9μm ozone band, the 10μm window, the 12μm H_2O band, the 5μm carbon monoxide band, the 4μm N_2O/CO_2 sounding region, and the 3μm window. The Michelson mirror travel is fixed at 1 cm maximum optical path difference, i.e. 0.5 cm^{-1} unapodized resolution. The optional fourth band would extend the resolution down to 0.33 cm^{-1} in the 15μm CO_2 temperature sounding region. The interferogram sampling is

controlled by an on-board solid state laser. The conceptual interferometer design uses corner mirror reflectors in place of flat mirrors with dynamic alignment. The ITS sounder has onboard blackbody calibration sources and requires a space view for the cold calibration target. The mask over the detectors define the nine fields of view of the instrument. The volume is expected to be comparable to that of the HIRS filter radiometer currently used on NOAA low earth orbiting satellites. The detailed implementation and power/mass budgets need to be determined in Phase A and B studies.

The ITS will scan the Earth viewing sector a total of 99.00° (±49.5° from nadir). The ITS total scan cycle time, which includes three lines of Earth viewing elements, internal calibration blackbody and space views, will be 8.0 seconds. At the end of the eight seconds the scan will be ready to begin the next scan cycle. The repeat time is required to be in synchronization with the scan line time of the AMSU-A Microwave Temperature Sounder, which is eight seconds (three scan lines of the AMSU-BE covering the same area will also be achieved in 8 seconds). The Earth viewing portion of the scan will be designed to provide one field-of-view for each of the AMSU-BE sounder's fields-of-view. The field of view pattern of the AMSU-BE is shown in Figure 8.

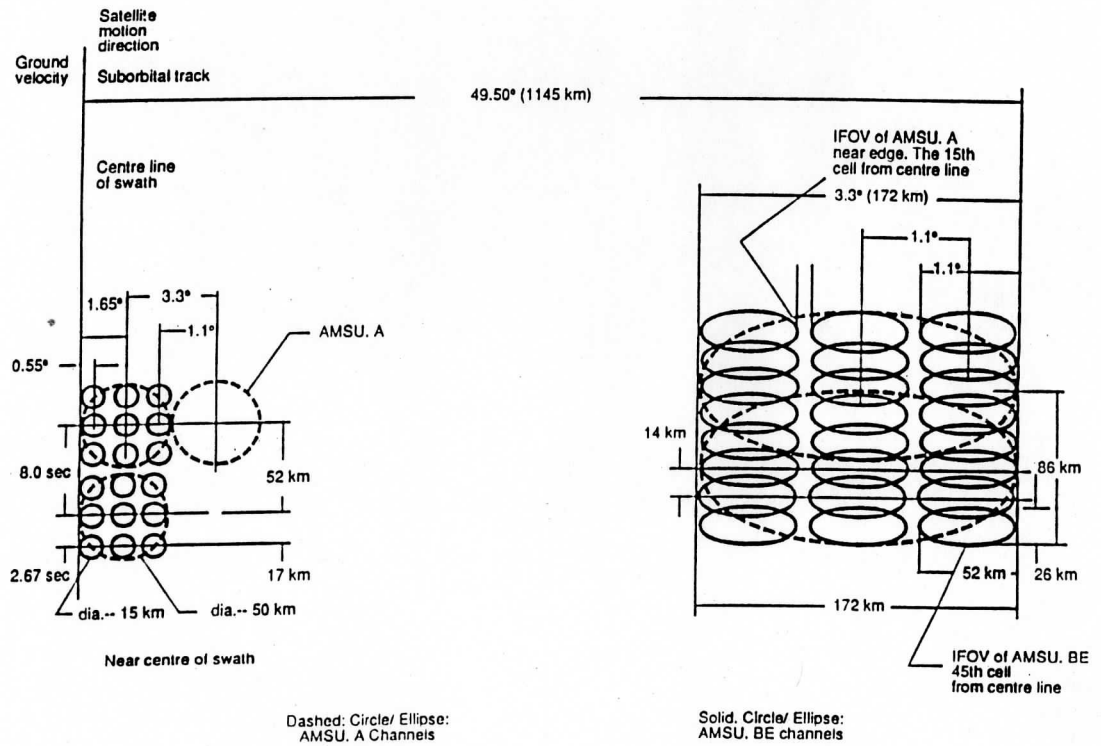

Figure 8. AMSU IFOV Overlay Pattern (showing one-half of swath)

3.32 ITS Radiometric Performance

In the low earth orbit design, collecting enough energy is no problem. The principal driver is the time available to perform the cross-track scan in order to match the ground spatial coverage of the AMSU-BE. Using 3x3 arrays to obtain nine fields of view in parallel and including the two calibration views plus the mirror retrace time, the ITS has 0.2 sec [= 8sec / (30 Earth View Clusters + 2 Calibration View Clusters + Retrace)] of dwell time available to make the interferometric measurements. This includes a 30 millisec step and settle time and 0.64 sec for Earth scan mirror retrace. With these constraints the expected noise performance is shown in Table 6 (refer to equation (1) in section 3.12 for the dependence of NEN on instrument parameters). The shorter dwell times in Bands 2 and 3 are meant to indicate the performance of those bands using only lower resolution data, though data of the same resolution as band 1 will be available for downlink. Though the design is only tentative, the radiometric performance of this conceptual design is quite good.

Table 6. Expected noise performance (apodized) for the ITS.

Band Name Minimum ν, cm^{-1} Maximum ν, cm^{-1}	**Band 1** 620 1150	**Band 2** 1210 1740	**Band 3** 2150 2720
NEN, $mW/m^2sr\ cm^{-1}$ @ Minimum ν @ Mid-band @ Maximum ν	 0.14 0.20 0.25	 0.034 0.042 0.048	 0.0051 0.0057 0.0064
NEΔT (260K), °C @ Minimum ν @ Mid-band @ Maximum ν	 0.10 0.16 0.25	 0.071 0.088 0.102	 0.17 0.18 0.21
Maximum OPD (cm)	1.0	0.5	0.2
Dwell Time (s)	0.2	0.1	0.05
Transmission, τ	0.24	0.24	0.24
D*peak, cm/Hz/W	3.5+10	1.0+11	3.8+11

3.33 ITS Sounding Performance

A sounding performance comparison of the low orbiter and the geostationary interferometer designs is shown in Figure 9. A comparison of the spectral coverage and spectral resolution of the Meteosat II sounder and the ITS indicates that the baseline design of the ITS should be roughly comparable in temperature and water vapor sounding capability to the medium resolution mode of the Meteosat II sounder. This comparable performance is shown in Figure 9a. The additional improvement of the high resolution mode of the Meteosat II sounder, shown in Figure 9b, could also be largely achieved by including the high resolution fourth band of the ITS described in section 3.31. The large improvement in vertical resolution of the baseline ITS over the performance of the filter wheel HIRS sounder is also apparent in Figure 9b.

Further study of the ITS design is necessary to provide important implementation details while maintaining the high level of temperature and water vapor sounding performance described here.

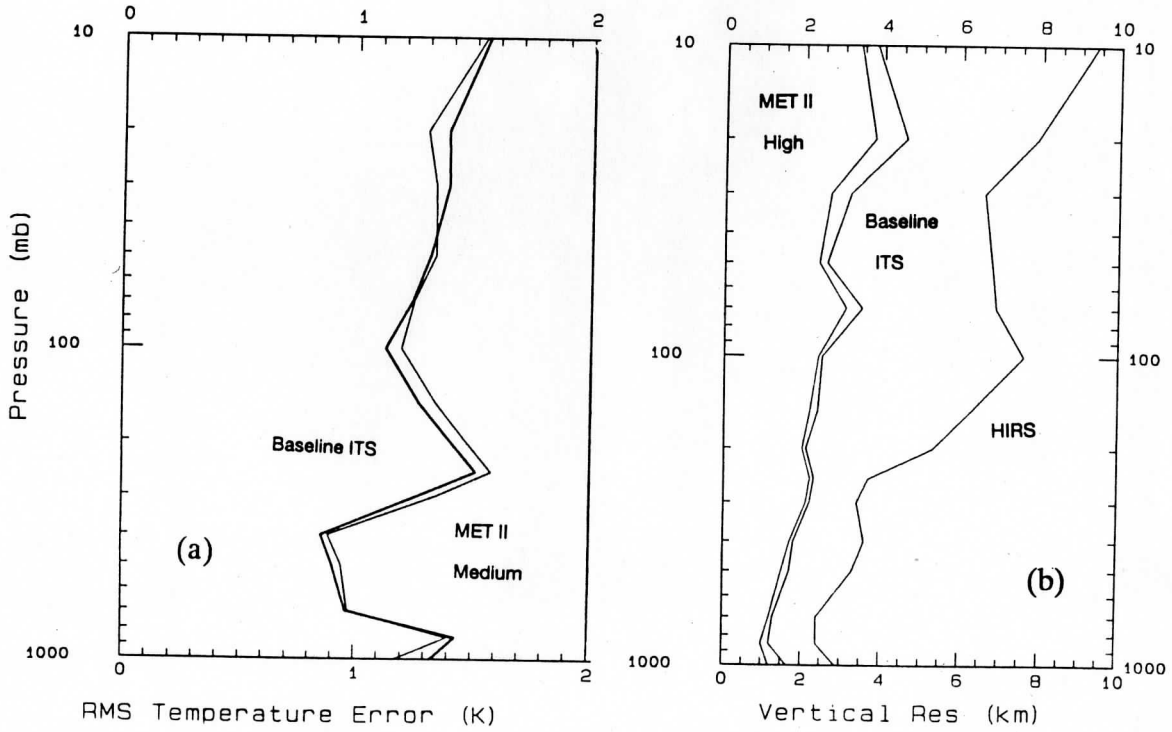

Figure 9. Comparison of geostationary and low earth orbiting interferometer sounding performance assuming the same spectral noise in (a) RMS temperature retrieval error, and (b) vertical resolution of temperature.

3.4 Interferometer Sounder Calibration Requirements

The discussion of calibration will concentrate first on the general approach and then on its implementation on the spacecraft. Note that the same calibration issues are present in both filter wheel and interferometric measurements. However, the interferometer has the advantage of a high degree of "channel-to-channel" wavenumber knowledge and stability.

The fundamental advantage of FTIR instruments for accurate calibration of emission measurements is their wavelength integrity, the same property which has made them the standard for very high resolution absorption measurements. The interferometer approach, coupled with laser triggered sampling, yields an instrument for which accurate central wavelengths and spectral weightings are mathematically defined from a few design parameters or a single adjustable parameter. As shown in Figure 10, the large slopes on the sides of lines can create large effective radiance errors for very small wavelength errors. Because of this, the importance of the extremely accurate wavelength calibration possible with FTIR increases with increasing spectral resolution.

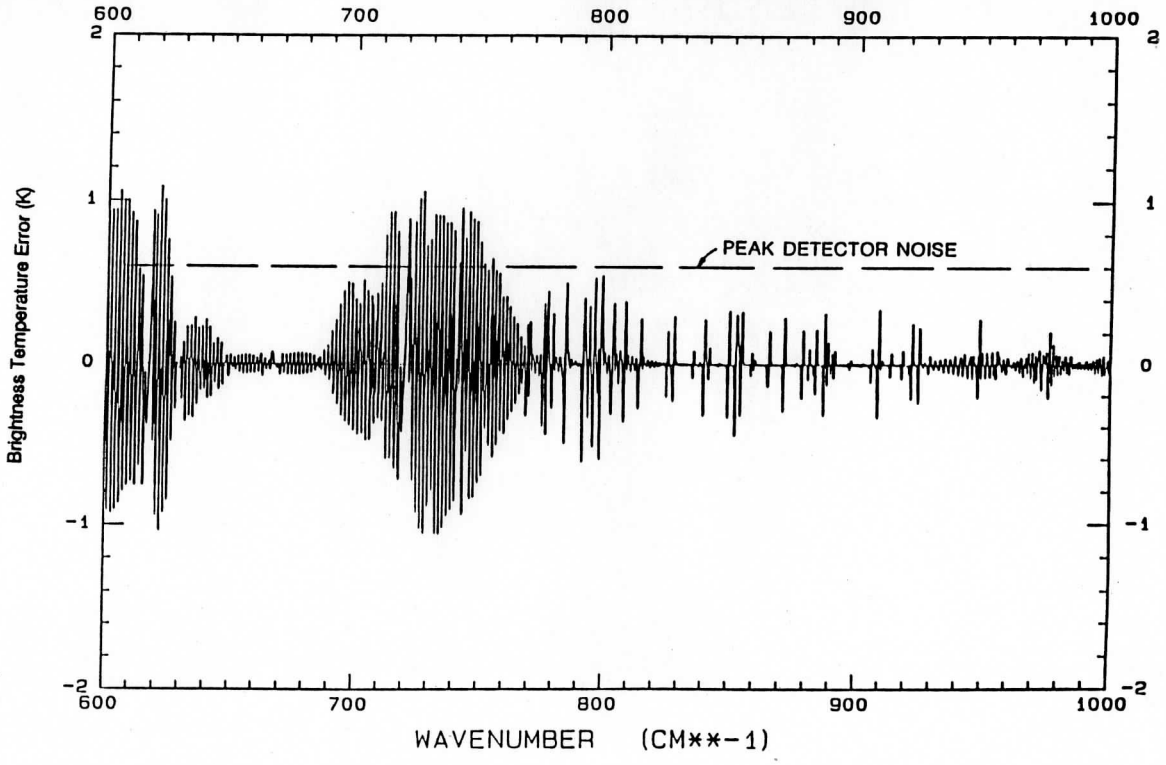

Figure 10. Spectral brightness temperature error caused by a shift of central channel wavelengths by 3% of $\Delta\nu$ for a spectrum with a resolving power of 1200. This points out the importance of the highly accurate interferometer wavelength calibration.

Experience with the High-resolution Interferometer Sounder (HIS) aircraft instrument has demonstrated that Fourier Transform - Infrared (FTIR) instruments are especially well suited to absolute emission measurements of broad spectral bands at high resolution (See HIS papers, Appendix B). Radiometric calibration of the HIS is accomplished with the same basic technique used in low resolution radiometry. Periodic viewing of two high emissivity, uniform temperature blackbody references provides the responsivity and offset parameters needed to convert measured spectra to radiances. Two blackbodies are adequate for the HIS because of the linearity of its detectors. One property which must be handled properly for accurate calibration of an interferometer is the phase. This topic is discussed in detail in the applied optics paper in Appendix B.

Laboratory verification of the HIS calibration consisted of the use of the instrument's 300 K blackbody and a liquid nitrogen blackbody to calibrate the spectrum of the instrument's second blackbody set for 260 or 280 K. It was consistently possible to retrieve the unknown blackbody temperature to within a few tenths of a degree across the whole spectral band except in regions of strong spectral absorption (about 1 m air path is included between the interferometer and the detector dewar assembly).

Atmospheric observations have verified that the HIS calibration is sufficiently accurate to serve as a standard for comparison with calculated radiances. The general agreement between HIS spectra and calculations from radiosonde temperature and water vapor profiles using the AFGL FASCOD2 program is remarkably good (see Fig 12, section 3.62), this is a tribute to the current state of line-by-line codes. However, spectroscopic deficiencies of several degrees Celsius are indicated by differences in many regions which are reproduced for very different atmospheres and observing conditions. Our comparisons with FASCOD2 have revealed other substantial differences resulting from trace gas absorption, CO_2 and H_2O line strength and/or line shape uncertainties, and from uncertainties in the strength of the H_2O foreign broadened continuum.

3.41 Calibration Sources

The Meteosat II sounder design incorporates an external blackbody source as indicated in Fig. 2. This source, of high emissivity and known temperature, will fill the instrument aperture with radiation of a known intensity during a calibration view. The blackbody is external, i.e. viewed by the same scene scan mirror optics used to view the earth, in order to be able to remove the effect of emission from each optical element. A view to cold space will provide the other calibration point. Space and the external blackbody will be viewed as often as necessary to compensate for internal instrument temperature drift. The frequency of this calibration will depend on the time rate of change of temperature of the emitting surfaces within the instrument

which will be closely monitored. Typically, a space view will be taken at the end of an earth raster scan line so as not to unnecessarily disrupt the mirror scan sequence. During periods of nominal instrument operation, external blackbody views will be made less frequently than views to space.

3.42 Calibration Equation

The equation used for calibration is the same as that used for a filter radiometer, with the exception that complex valued spectra (the FFT of double-sided interferograms) must be used instead of real valued spectra. In the end, the real part of the calibrated spectra contains the physical earth radiance. The imaginary part contains only noise centered about zero and is used as a diagnostic check on the calibration process.

The calibration equation which applies to each channel ν is

$$N^{cal}_{\nu} = C^{(1)}_{\nu} \cdot N^{earth}_{\nu} + C^{(2)}_{\nu} \qquad (2)$$

where the slope, $C^{(1)}$, and the offset, $C^{(2)}$, are given by

$$C^{(1)}_{\nu} = B_{\nu}(T_H)/(N^{H}_{\nu} - N^{space}_{\nu}), \text{ and}$$

$$C^{(2)}_{\nu} = -C^{(1)}_{\nu} \cdot N^{space}_{\nu}.$$

In these equations, N^H is the hot blackbody view, T_H is the temperature of the hot blackbody, B(T) is the Planck radiation function at temperature T, N^{space} refers to the deep space view, N^{cal} is the calibrated earth spectrum, and $(\cdot)$ represents the multiplication of complex quantities.

3.43 Calibration Specifications

The "cold" calibration target will be the cosmic background radiation (cold space). At the cold calibration position, the scan mirror should have a clear unobstructed view of cold space. The "hot" calibration target should be an instrument ambient target (nominally 300 Kelvin). The "hot" calibration target should be monitored to a precision of better than 0.1°C with a goal of 0.05°C. Uniformity of the "hot" target should be better than 0.5°C. Emissivity of the "hot" calibration target should achieve a calculated effective emissivity of 0.9970 or greater.

Calibration accuracy and repeatability are defined as the difference (error) between the brightness temperature inferred from the sensor and the actual temperature of a blackbody test target directly in front of the scan mirror. The absolute error should be $\leq$ 1°C (at 260 K for wavelengths larger than 5 μm and at 280 K for smaller wavelengths). Inter-channel calibration error should be less than 0.2°C. Inter-channel calibration error is defined as the difference between any two channel outputs (expressed in units of brightness temperature and averaged sufficiently to make noise negligible) when viewing the same constant-temperature scene.

The requirements on wavelength calibration (i.e. laser wavelength accuracy and stability) follow from these basic radiometric calibration specifications.

3.5 Impact of Scene Variations on Interferometric Data

This section contains a discussion of the impact of variations in the scene during an interferometer measurement scan. The following sections describe the nature of the problem, experience with the HIS aircraft instrument, and the solution proposed for satellite instruments.

3.51 Description of the Problem

Unlike a filter wheel radiometer, which integrates spectral radiance over channels sequentially, an interferometer measures all wavelengths within its optical bandpass simultaneously. During a single observing time period, the Michelson interferometer moving mirror samples a range of optical path differences (OPDs) from one side of zero path difference to the other. In doing so the interferometer is measuring "low resolution" Fourier components near zero path difference (ZPD), and "high resolution" components as the Michelson mirror moves away from ZPD. If during this time of OPD scan the scene should change, then the low resolution component of the scene and the high resolution components could be inconsistent with each other. The details of the spectral distortions that result depend entirely on the frequency and amplitude of the scene variations present, but for typical cases (e.g. partly cloudy, partly clear scenes) the nature of the effect is to enhance the "noise" level in portions of the spectrum that have the most rapid spectral variations.

There are two cases of particular interest as far as scene variations are concerned. The first case is when the change in the scene is a linear function of time. This is applicable to the case of a measurement from a moving aircraft, or motion along the suborbital direction from a low earth orbiting satellite. In this important case, there is no error associated with the Michelson interferometer measurement as long as measurements are made on either side of zero path difference and the change in scene is a linear function of time. The Fourier Transform of the double sided interferogram will then give the same result as that of an instrument that observed the same linearly varying scene directly in the spectral domain. The second case is that of random scene mirror "jitter", such as might be present in an optical system using a "step and settle" mirror system. This case is appropriate to either the three axis stabilized geostationary instrument or to the "cross-track" scan of the low earth orbiting instrument. In this case, the tolerance on settle time, and the residual frequencies must be carefully controlled so as to minimize the effects of these induced scene variations.

3.52 High-Altitude Aircraft Experience

Since its development and testing in 1985, the High-resolution Interferometer Sounder has flown on over 40 separate flight missions with the NASA high-altitude research platform, the U2/ER-2 aircraft. Data taken with this instrument has been used repeatedly for scientific demonstration of the retrieval capabilities of high resolution interferometeric data without any significant problem with scene variations of the type described in 3.51. The HIS instrument has a single fixed (non-scanning) nadir viewing field of view with a 2 km footprint from an aircraft altitude of 20 km. The total integration time for a single scene is 6 seconds for a complete double sided interferogram scan of ±1.8 cm OPD. The uncompensated scene motion is 30% of the FOV relative to ZPD. The presence of error due to scene variation is difficult to distinguish from other instrument and atmospheric noise sources which are of equal or greater magnitude.

3.53 Expectation for Satellite Platforms

The nature of the problem of scene variations is well understood. In the satellite instruments from both geostationary and low earth orbits, a proper design would provide for scene motion compensation in the scene mirror optical design, with a tolerance on the scene mirror step and settle times and frequencies required to guarantee that scene variation errors are small compared to other error sources. A simulation of the expected errors is shown in Figure 11.

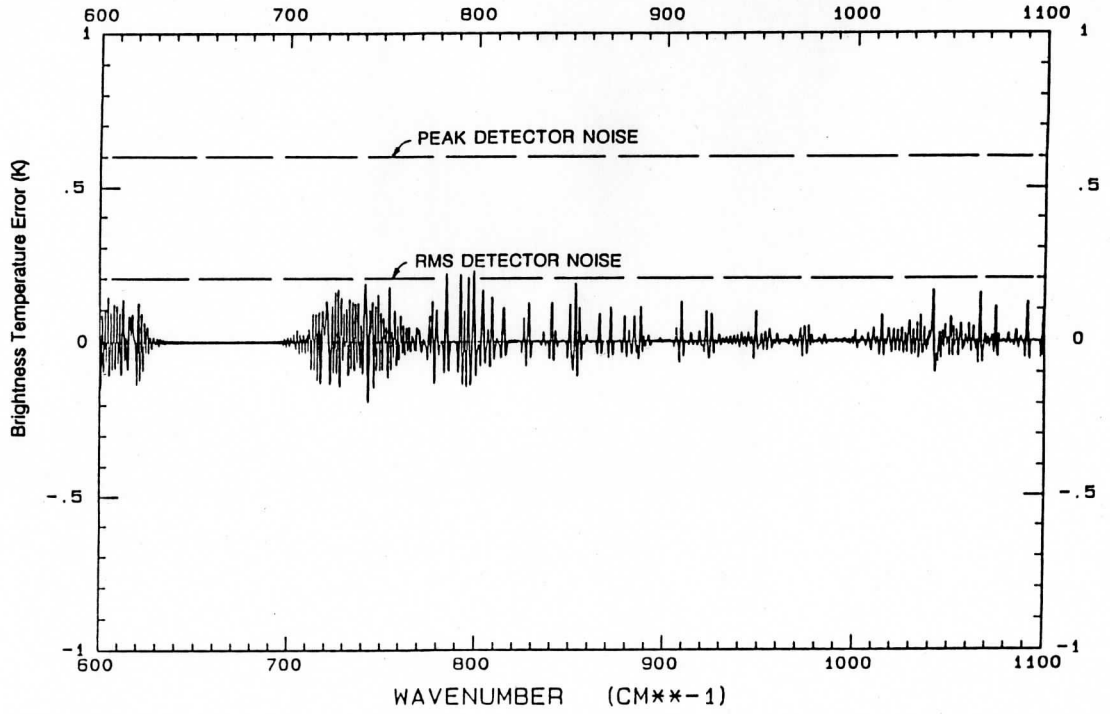

Figure 11. Peak error from a statistical simulation of scene variations (1% of FOV) over land with randomly varying mixed clear (300K) and cloud (250K) scenes.

The baseline designs presented in this report include scene mirror motion compensation. Without compensation the low earth orbiting design would have an scene motion of 10% of the FOV relative to ZPD. With a small flexure of the 45° scan mirror, the uncompensated residual is reduced to 1-3% with frequencies of less than 50 Hz. Figure 11 shows that the magnitude of the peak errors for 1% uncompensated scene motion across the long wavelength spectral band are much less than the rms detector noise levels and thus are insignificant. There is no error from DC-level variations which occur at frequencies well below the lowest information frequency of 4 KHz.

3.6 Noise Specifications for an Interferometer Sounder

This section describes the treatment of noise for a Michelson interferometer design and contrasts it to the noise specifications frequently applied to filter radiometers. The issues discussed in the following are noise in the Fourier domain, the variation of spectral noise with wavelength when expressed in equivalent temperature, and the specific sensitivity characteristics of the HgCdTe detectors proposed in the baseline interferometer designs.

3.61 Noise in the Fourier vs Spectral Domains

One of the key differences between a radiometer that measures spectral radiation directly and a Michelson interferometer is that the interferometer makes measurements in the Fourier domain and thus the noise on those measurements is also in the Fourier domain. The set of measurement points that make up the interferometric measurement for a single field of view is called the interferogram. Each point in the interferogram has measurement noise associated with it. The complete set of points in the interferogram is simply related to the actual infrared spectrum by a Fourier Transformation. In the same way, measurement noise in the Fourier domain can be transformed to the spectral domain and thereafter considered to be "spectral" noise. In fact, random noise uniformly distributed in the Fourier domain will be transformed through Fourier Transformation into random noise uniformly distributed across the spectral domain.

3.62 Spectral Brightness Temperature Variability

In general terms, noise is uniformly distributed in the interferogram (Fourier domain), and hence is uniformly distributed in radiance (roughly flat) across each one of the separate spectral bands. However, radiometric performance is often specified in terms of equivalent blackbody

temperature which implies the need to specify a "typical" scene temperature at which the NEdT specification applies. Interferometric data of the type described here differ in two ways from the data commonly obtained from filter radiometers. The first difference is that the high spectral resolution within each band means that the absorption lines of molecular constituents of the atmosphere cause large variations in equivalent brightness temperature in nearby regions of the spectrum, as shown in Fig. 12. The second difference is that the wide spectral bands ($> 500\ cm^{-1}$) mean that the Earth emitted Planck radiation curve falls significantly from the long wavelength to the short wavelength end of each band. The net effect of these two characteristics of interferometric data is that no single specification of radiance or brightness temperature applies equally to all spectral channels. The specification of a single radiance requirement on a band implies a higher signal to noise on the long wavelength end than on the short wavelength end of the same band. Similarly, the specification of a single equivalent brightness temperature requirement is not adequate to characterize the wide variations in effective temperature that the instrument sees in nearby spectral channels. Some compromise in the specification of requirements is necessary. The compromise that has been adopted here is to specify a single noise equivalent temperature, NEdT, for each interferometer band, but to have it apply only in an average sense across the band, and with a higher reference temperature for the short wavelength band(s).

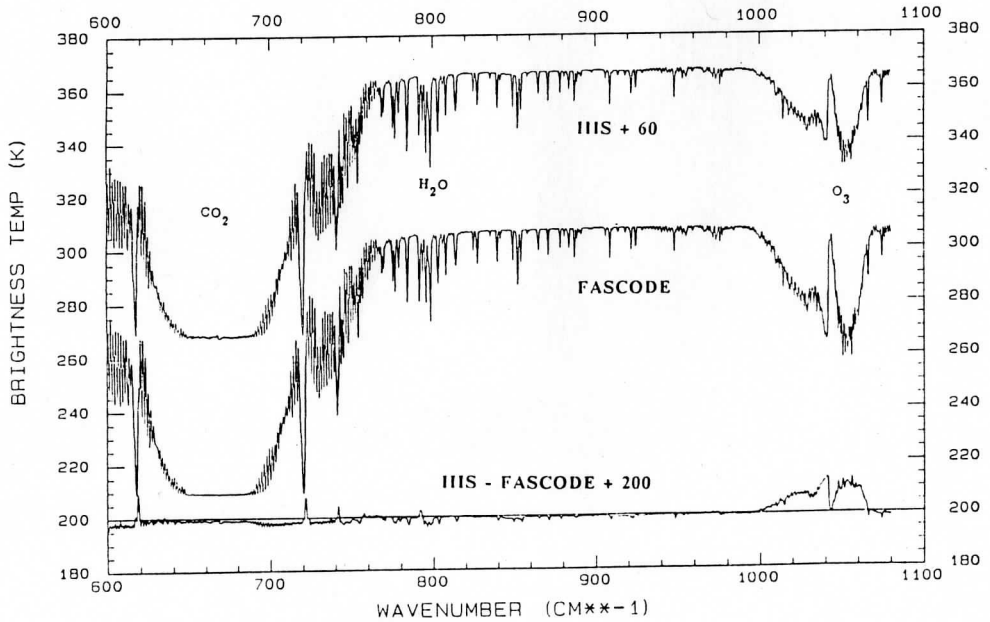

Figure 12. Atmospheric blackbody equivalent temperature from HIS measurement compared to a FASCOD2 calculation showing large effective temperature variations within a single measurement band.

3.63 Detector Characteristics

The character of the proposed HgCdTe detectors is that the response can be peaked at a particular wavelength, but that the detector response falls off rapidly away from the peak. A typical D* curve of for an HgCdTe detector is shown in Figure 13. The strategy that has been followed in the baseline designs presented here has been to peak the detector response of each set of detectors toward the long wavelength end of each spectral band. The NEN simulations assume a decrease in D* linear in wavelength within each band.

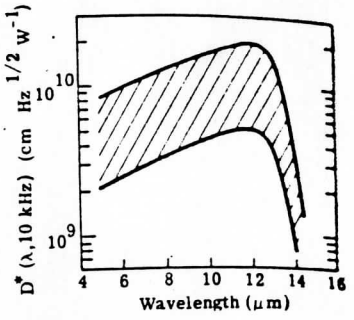

Figure 13. D^* for a HgCdTe detector from the Infrared Handbook.

The spectral bands have been chosen appropriately to enhance the scientific return of this measurement requirement. The result of this physical characteristic of the detector is that the sensitivity of the detector response to radiation is smaller on the short wavelength end of each band. This fact, combined with the falloff of the Planck function with increasing wavenumber, explains why the expected noise performance has the characteristic shape that can be seen in Figure 3, with a degradation of performance on the short wavelength end of each band.

3.7 Sounder Data Compression Techniques

To fulfill the desire for high vertical resolution soundings requires the measurement of high spectral resolution data with a corresponding increase in the data rate from instruments, such as the interferometer, which make such measurements. The data stream from the interferometer sounder requires several levels of data processing, each of which tends to decrease the data volume. The choice of how much data processing to do on-board the spacecraft versus how much to do on the ground needs to be made in the context of the available downlink data rate and data storage requirements. Three techniques will be discussed that can be used to decrease the volume of the interferometric data both for transmission purposes and for reducing archival storage requirements. These three techniques are onboard digital filtering/FFTs, information compression, and pseudo-profile techniques.

3.71 On board Fast Fourier Transforms

The internal data rate of the interferometer is determined by the wavelength of the onboard laser used to control the sampling of the interferogram. The standard practice is to oversample

the interferogram at or near the laser rate (9434 samples/cm OPD), then to convolve the digitized samples with a numerical filter. The digital filtering provides a volume reduction of approximately an order of magnitude, bringing the data volume down to the minimum necessary to contain the information content of the interferogram. This is a natural point at which to downlink the interferometer sounder data (typically 1.0-1.5 Mbps). The next step in the data processing is to perform a fast fourier transform on the numerically filtered interferogram. The details of the transform depend on the exact band edges chosen and the type of convolving filter applied, but typically the FFTs are made on 2K or 4K complex data points. The small size of this transform is what allows this processing step to be easily accomplished on the spacecraft using standard digital signal processors or on the ground after the downlink of the interferograms. After the transform to the spectral domain another volume reduction in the data is possible by making use of channel selection and/or data compression. The data rate of the spectral data can be easily obtained by multiplying the number of spectral channels per field of view by the number of bits per channel and by the number of fields of view then dividing by the time available. An additional factor of two reduction is possible by considering magnitude spectra only. This is possible only when the spectral phase is well known and stable from spectra to spectra. The typical data rates for the interferometer sounder after FFT and channel selection are 0.5-1.0 Mbps.

3.72 Information Preserving Compression

Several generic techniques exist for compressing digitized data without loss of information content which promise to provide a compression factor of 3 or more. The sounder data stream is characterized by nine simultaneous measurements, each of which is a sequence of oscillatory data points (whether interferograms or high resolution spectra). This data may be decomposed into orthogonal functions and the coefficients of the decomposition and the residuals with the actual measurements downlinked or stored. The effectiveness of this scheme depends on the suitability of the choice of orthogonal function to the type of data being decomposed. Alternatively, a differencing scheme could be applied to either the sequence of channels within a single field of view or to the differences between the same spectral channels using adjacent fields of view with the difference between the numbers transmitted in place of the numbers themselves. Any differencing scheme will work best when the differences between the numbers being compared is small.

The careful study of the compression factors possible with real data (such as from the HIS) needs to be carried out in the context of its application to satellite data transmission. This is an area for future study.

3.73 Pseudo-Profile Compression Technique

This technique relies on the way the data will be processed to produce sounding information and makes use of the considerable data reduction that occurs when going from the 4000 or so spectral channels down to the 40 or so retrieved levels of temperature and water vapor. The linear perturbative solution to the equation of radiative transfer can be written as

$$T_{(Lx1)} = D_{(LxL)} * W_{(LxN)} * R_{(Nx1)},$$

where T is a vector containing retrieved temperature at L levels, R is a vector containing radiance measurements at N spectral channels, D is a square LxL matrix known as the deconvolution matrix, and W is a rectangular (LxN) matrix whose columns contain the weighting functions appropriate to the retrieved quantity. The symbol * stands for the matrix product. Notice that the product W*R is an Lx1 vector, where L is about 40, compared to the Nx1 measurement vector R, where is N is greater than 4000. Thus a volume (and data rate) savings of about two orders of magnitude are possible if the weighting function matrix W is applied to R before satellite downlink. The practicality of uploading a set of weighting function matrices to the satellite is an area for future study, but the advantages to operational temperature and water vapor sounding data rate and volume may be quite large.

4.0 Summary

This report has presented a series of issues relating to sounding the atmosphere with interferometer instruments. The tradeoffs among spectral resolution, noise, telescope aperture, dwell time, and area coverage have been discussed throughout. The specific topics that have been discussed are summarized below.

An interferometer design for the Meteosat II sounder has been presented and the instrument noise performance and operating mode flexibility have been described. Sounding retrieval performance simulations were also presented which show that the baseline design meets the need to improve the retrieval of temperature and water vapor to the level of 1°C and 10%, respectively, with 1 km vertical resolution in the lower atmosphere. It has been shown how a flexible instrument design allows the tradeoffs of dwell time, resolution, and area coverage to be made by the operational user of the instrument to satisfy the needs of the many meteorological applications foreseen for the geostationary instrument. The interferometer has the unique capability of easily allowing the sort of operational flexibility which would be very difficult to obtain in any other way.

A concept for a low earth orbiting interferometer (the ITS) has been described and its performance compared to the current filter wheel instrument (the HIRS). The conceptual

instrument design makes use of the increased signal strength of the earth emitted radiance viewed from low orbit to allow a compact instrument with an envelope very similar to the current HIRS design. Due to the constraints of dwell time and spatial synchronization with the AMSU-BE, the low earth orbiting design has less flexibility than the geostationary design, but makes optimum use of the available spectral information to obtain nearly the same sounding performance as the Meteosat II interferometer sounder. The ITS would be a great advance in meteorological measurements over any currently available operational thermodynamic instrumentation.

The calibration requirements of the interferometer sounders has been shown to be the same as that required for filter wheel radiometer sounders. The additional requirement for channel center wavelength knowledge imposed by high resolution data is also easily obtained with the interferometer which uses laser controlled sampling to obtain a very well defined sampling of the radiance spectrum.

The issue of scene variations during an interferometer optical path difference measurement has been discussed. It has been argued that with careful earth scan mirror design any spectral artifacts can be avoided. Moreover, observations with the HIS aircraft instrument have shown that even large scene variations have a relatively modest impact on actual observations.

The specification of noise requirements has been addressed. It has been suggested that radiometric noise specifications be made on each band of the interferometer, expressed as a noise equivalent temperature NEdT at a scene temperature appropriate for the wavelength region being considered. The NEdT specification is to be applied in an average sense over the wide spectral band. Specifically, the NEdT specification is to be met at mid band. Then typically, NEdT will be smaller at the long wavelength end of the band, and larger at the short wavelength end.

It has also been shown that techniques exist for reducing the volume of interferometric data by several orders of magnitude. The specific techniques to be applied need to be chosen in the context of the degree of on-board processing needed versus downlink data rate, storage, and user product requirements.

In conclusion, the interferometer sounder, in both its geostationary and low earth orbiting configurations, can provide the increase in vertical resolution and RMS temperature and water vapor retrieval needed to meet the requirements of a Twenty First Century meteorological operational environment.

5.0 Bibliography

Ackerman, S.A., W.L. Smith, J. Spinhirne, and H.E. Revercomb, 1990a: **The 27-28 October 1986 FIRE IFO Cirrus Case Study: Spectral Properties of Cirrus Clouds in the 8-12 micron Window**, Monthly Weather Review, in press, 1990.

Ackerman, S.A., E.W. Eloranta, C.J. Grund, R.O. Knuteson, H.E. Revercomb, W.L. Smith, and D.P. Wylie, 1990b: **University of Wisconsin Cirrus Remote Sensing Pilot Experiment.** 7th Conference in Atmospheric Radiation, 24 July 1990, San Francisco.

Clough, S.A., R.D. Worsham, W.L. Smith, H.E. Revercomb, R.O. Knuteson, H.W. Woolf, G.P. Anderson, M.L. Hoke, and F.X. Kneizys, 1988: **Validation of FASCODE Calculations with HIS Spectral Radiance Measurements.** International Radiation Symposium, Lille, France.

Grund, C.J., E.W. Eloranta, D.P. Wylie, and H.E. Revercomb, 1990: **Lidar and Radiometric Observation of Local and Mesoscale Cirrus Cloud Properties with High Spectral and Spatial Resolution.** 15th International Laser Radar Conference, Tomsk, USSR, 23-27 July 1990a.

Grund, C.J., S.A. Ackerman, E.W. Eloranta, R.O. Knuteson, H.E. Revercomb, W.L. Smith and D.P. Wylie, 1990b: **Cirrus Cloud Characteristics Derived from Volume Imaging Lidar, High Spectral Resolution Lidar, HIS Radiometer, and Satellite.** 7th Conference on Atmospheric Radiation, AMS, San Francisco, CA, 23-27 July 1990.

Revercomb, H.E., H. Buijs, H.B. Howell, R.O. Knuteson, D.D. LaPorte, W.L. Smith, L.A. Sromovsky, and H.W. Woolf, 1987/1989: **Radiometric Calibration of IR Interferometers: Experience from the High-resolution Interferometer Sounder (HIS) Aircraft Instrument.** RSRM '87:Advances in Remote Sensing Retrieval Methods, A. Deepak, H. Fleming, J. Theon (Eds.). A. Deepak Publishing, Hampton, Virginia.

Revercomb, H.E., D.D. LaPorte, W.L. Smith, H. Buijs, D.G. Murcray, F.J. Murcray, and L.A. Sromovsky, 1988a: **High-Altitude Aircraft Measurements of Upwelling IR Radiance: Prelude to FTIR from Geosynchronous Satellite.** Mikrochimica Acta [Wien], II, 439-444.

Revercomb, H.E., H. Buijs, H.B. Howell, D.D. LaPorte, W.L. Smith, and L.A. Sromovsky, 1988b: **Radiometric Calibration of IR Fourier Transform Spectrometers: Solution to a Problem with the High Resolution Interferometer Sounder.** Applied Optics, 27, 3210-3218.

Revercomb, H.E., W.L. Smith, L.A. Sromovsky, R.O. Knuteson, H. Buijs, D.D. LaPorte, and H.B. Howell, 1989a: **Radiometrically Accurate FTS for Atmospheric Emission Observations.** Proceedings 7th International Conference on Fourier Transform Spectroscopy, SPIE Volume 1145, edited by David G. Cameron.

Revercomb, H.E., W.L. Smith, R.O. Knuteson, H. M. Woolf, and H.B. Howell, 1989b: **Comparisons of FASCODE Spectra with HIS Observations.** Proceeding of the AFGL Annual Review Conference on Atmospheric Transmission Models, 5-7 June.

Revercomb, H.E., R.O. Knuteson, W.L. Smith, H. M. Woolf, and H.B. Howell, 1990: **Spectroscopic Inferences from HIS Measurements of Atmospheric Thermal Emmission.** Optical Remote Sensing of the Atmosphere, 1990 Technical Digest Series, Vol 4, from Topical meeting, Incline Village, Nevada, 12-15 February, published by the Optical Society, Washington, DC, 590-593.

SBRC, 1981: **A Design Feasibility Study for the High Resolution Interferometer Sounder (HIS)**, SBRC (75 Coromar Drive, Goleta, CA) Report to the University of Wisconsin, Updated July 1982 and February 1983.

Smith, W.L., H. E. Revercomb, H. B. Howell, and H. M. Woolf, 1983: **HIS - A Satellite Instrument to Observe Temperature and Moisture Profiles with High Vertical Resolution**, in Fifth Conference on Atmospheric Radiation, American Meteorological Society, Boston Mass.

Smith, W.L., H.E. Revercomb, H.M. Woolf, H.B. Howell, D.D. LaPorte, and K. Kageyama, 1987a: **Improved Geostationary Satellite Soundings for the Mesoscale Weather Analysis/Forecast Operations**, in Proc. Symp. on Mesoscale Analysis and Forecasting, Vancouver, Canada, 17-19 August, ESA SP-282, 79-83.

Smith, W.L., H.M. Woolf, H.B. Howell, H.E. Revercomb, and H.-L. Huang, 1987b: **HIS - A High Resolution Atmospheric Sounder**, 21st International Symposium on Remote Sensing of Environment, Ann Arbor, Michigan, 26-30 October.

Smith, W.L., H.M. Woolf, H.B. Howell, H.-L. Huang, and H.E. Revercomb, 1987/1989: **The Simultaneous Retrieval of Atmospheric Temperature and Water Vapor Profiles - Application to Measurements with the High-resolution Interferometer Sounder (HIS).** RSRM '87:Advances in Remote Sensing Retrieval Methods, A. Deepak, H. Fleming, J. Theon (Eds.). A. Deepak Publishing, Hampton, Virginia.

Smith, W.L., H.M. Woolf, H.B. Howell, H.E. Revercomb, and H.-L. Huang, 1988a: **High Resolution Interferometer Sounding - The Retrieval of Atmospheric Temperature and Water Vapor Profiles**, in Proc. Third Conference on Satellite Meteorology and Oceanography, (Anaheim, California, 1-5 February 1988a), AMS, Boston, MA.

Smith, W.L., H.E. Revercomb, H.B. Howell, and M.-X. Lin, 1988b: **Multi-spectral Window Radiance Observations of Cirrus from Satellite and Aircraft - November 2, 1986 "Project FIRE".** FIRE Conference, 11-15 July.

Smith, W.L., H.-L. Huang, H.E. Revercomb, A.J. Schreiner, and H.M. Woolf, 1989: **Future Satellite Sounding Techniques.** Presented at the ECMWF/EUMETSAT Workshop, Reading, U.K., 6-13 May 1989.

Smith, W.L., et al., 1990a: **GAPEX: A Ground-Based Atmospheric Profiling Experiment.** BAMS, 71, 310-318.

Smith, W.L., H. E. Revercomb, D.D. LaPorte, L.A. Sromovsky, S. Silverman, H.M. Woolf, H.B. Howell, R.O. Knuteson, and H.-L. Huang, 1990b: **GHIS - The GOES High Resolution Interferometer Sounder.** GOES I-M Operational Satellite Conference, 3-6 April 1989, and JAM, in press.

Smith, W.L., H. E. Revercomb, and H.M. Woolf, 1990c: **A Linear Simultaneous Solution for Temperature and Absorbing Constituent Profiles from Radiance Spectra.** Applied Optics, in review.

Smith, W.L., H.-L. Huang, H. E. Revercomb, and H.M. Woolf, 1990d: **On the Combination of Passive and Active Sensing for Achieving Very High Resolution Atmospheric Temperature Profiles.** Optical Remote Sensing of the Atmosphere, 1990 Technical Digest Series, Vol 4, from Topical meeting, Incline Village, Nevada, 12-15 February 1990, published by the Optical Society, Washington, DC, 198-201.

Smith W.L., H.-L. Huang, and H.E. Revercomb, 1990e: **Sounding through Semi-transparent Cloud with High Resolution Infrared Radiance Spectra.** 5th Conference on Satellite Meteorology and Oceanography, 3-7 September 1990, London, England.

UW/SBRC/ITT, 1988: **High Resolution Interferometer Modification of the GOES L/M Sounder: Feasibility Study**, Report to NOAA/NESDIS, September 1988.

APPENDIX A: DWELL TIME DEPENDENCE OF SIMULATED SOUNDINGS

APPENDIX A: Dwell Time Dependence of Simulated Soundings

For the purposes of this study, detailed simulations of temperature and water vapor retrieval error and of vertical resolution have been computed for each of the baseline resolution modes of the Meteosat II sounder (see Table 3 in Section 3.13) at several spectral noise (NEdT) levels. Recall Section 3.2 on sounding retrieval performance. A layer average of rms retrieval errors was computed in order to characterize two important regions of the atmosphere. A 700-1000mb layer average was computed to demonstrate retrieval accuracy for both temperature and water vapor in the lower troposphere. A 200-300mb layer average was also computed for rms temperature retrieval error as a "worst case" example. In order to parameterize the spectral noise (NEdT) dependence of the retrievals, the temperature and fractional precipitable water retrieval errors have been empirically fit to an analytical function of the form

$$F(r) = a\,(1 - \exp[-r/c]) + b\,r + d$$

where r is the spectral noise level (NEdT) in degrees Celsius, F is the retrieval error function to be fit (either rms temperature error, or fractional precipitable water error), and a, b, c, and d are constants adjusted to obtain a best fit in each case. All the resolution modes were fit well by this empirical function. The advantage of this analytic form is that a transformation of variables into sounding dwell time and subsequent comparison of various operating modes is greatly simplified. This transformation of variables was made by assuming that detector noise is inversely proportional to the square root of the avaiable dwell time (for dwell times equal to a multiple of the basic integration time for that mode). For example, a 1 sec dwell sounding in high resolution mode could be directly compared in this way to ten 0.1 sec soundings made sequentially in low resolution mode.

Note that equation (1) of Section 3.12 implies that, for a fixed dwell time, NEdT is directly proportional to maximum OPD travel (X). Thus one would expect that for the same dwell time that medium resolution mode would have an NEdT one half that of high resolution mode, and moreover, low resolution mode would have an NEdT one fifth that of medium. That this is true can be seen from a plot of NEdT detector noise versus dwell time shown in Fig. A-1(a) for each of the operating modes; high, medium, and low. However, in the real world, there are sources of noise beyond detector noise that also influence the ability of a retrieval algorithm to generate accurate retrievals. Some of these sources may be instrumental, some may be atmospheric (clouds, haze, inversions, turbulence), some may be due to uncertainties in the molecular

spectroscopy, and some may be due to numerical quadrature errors. All such errors that are both independent of the length of time spent dwelling in one spot and independent of spectral resolution will be referred to as "fixed" noise in the remainder of this report. A simple, but more realistic, parameterization of NEdT is presented below:

$$\text{NEdT}(t)^2 = \text{Detector Noise}(t)^2 + (\text{"Fixed" Noise})^2,$$

where Detector Noise(t) refers to the equation for NEN in Section 3.12. This relation is illustrated in Fig. A-1(b) for a fixed noise level of 0.1°C. The value of 0.1°C is thought to be a reasonably typical value given the current understanding of noise sources. In any actual case the fixed noise level may be greater or less.

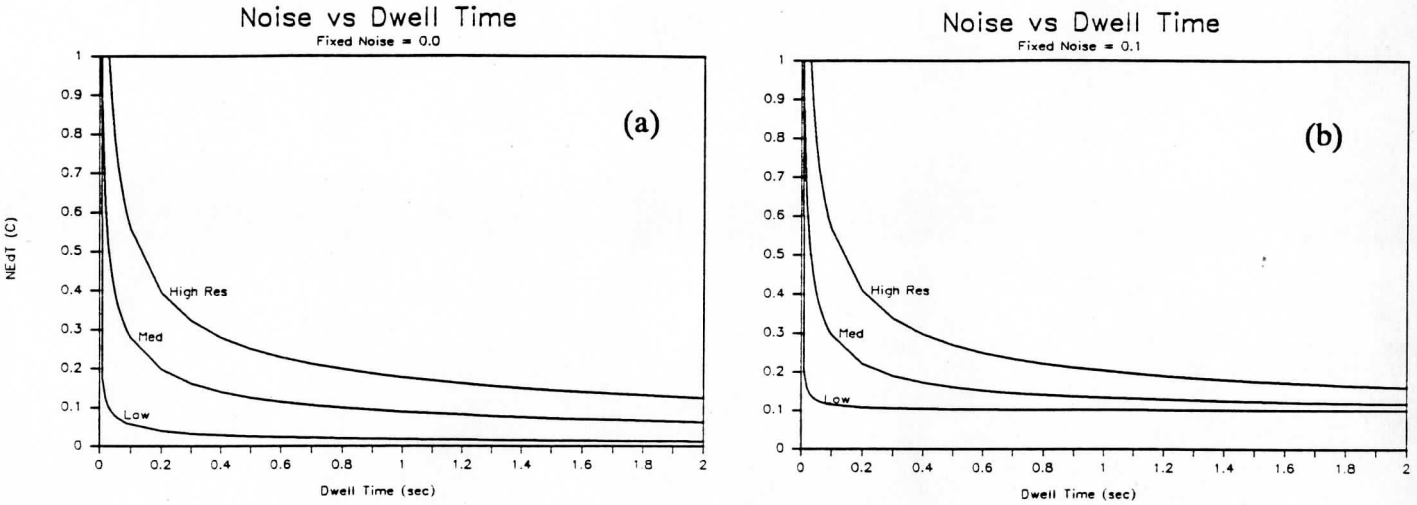

Figure A-1. NEdT vs Dwell Time for (a) zero fixed noise and (b) non-zero fixed noise.

The comparison of retrieval errors versus sounding dwell time is shown in Figs. A-2 to A-4. Figure A-2 shows the dependence of rms temperature error and the fractional precipitable water error versus dwell time for the various modes of an ideal sounder with no fixed noise. In general, these curves show that, with an ideal sounder, low resolution mode gives better performance than high resolution for short sounding dwell times and comparable performance at longer sounding dwell times. However, in the more realistic case shown in Figs. A-3 we see that, with non-zero fixed noise, medium and high resolution modes consistently outperform the low resolution mode. The same conclusions follow from consideration of the 200-300mb "worst case" example shown in Figs. A-4.

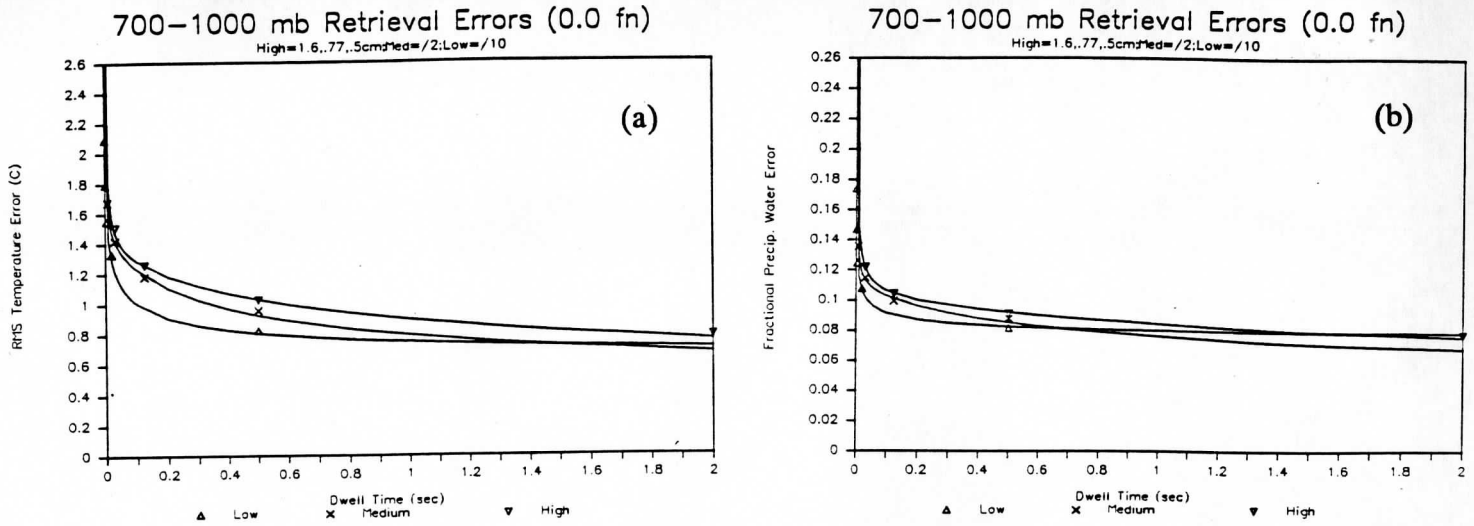

Figure A-2. Retrieval Error vs Dwell Time without fixed noise. 700-1000 mb.

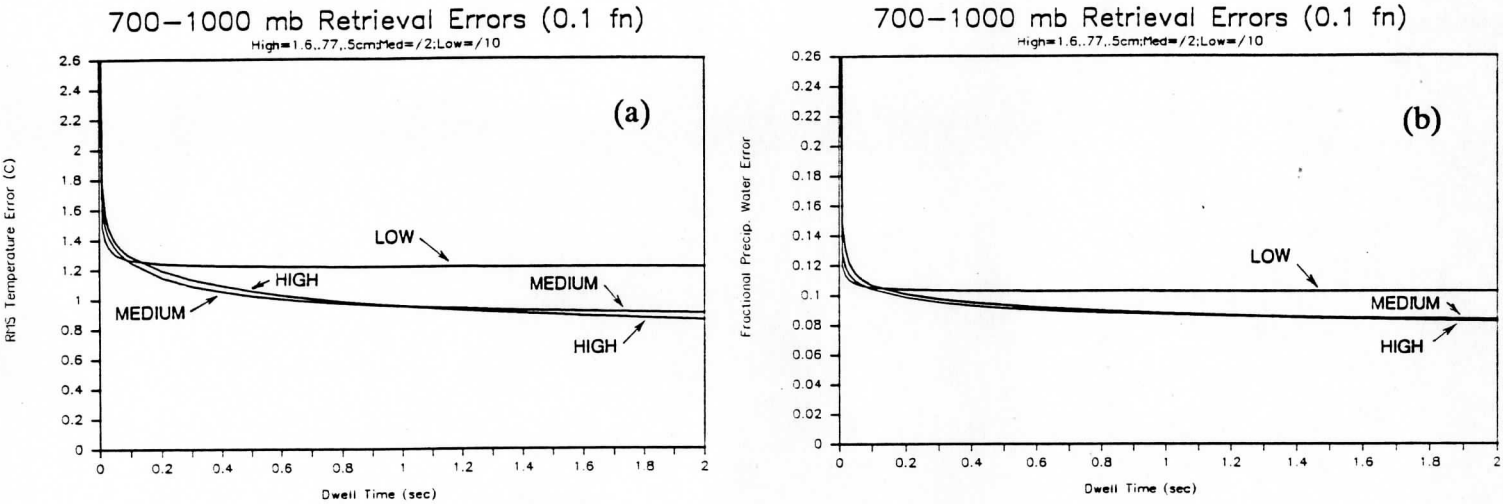

Figure A-3. Retrieval Error vs Dwell Time with fixed noise. 700-1000 mb.

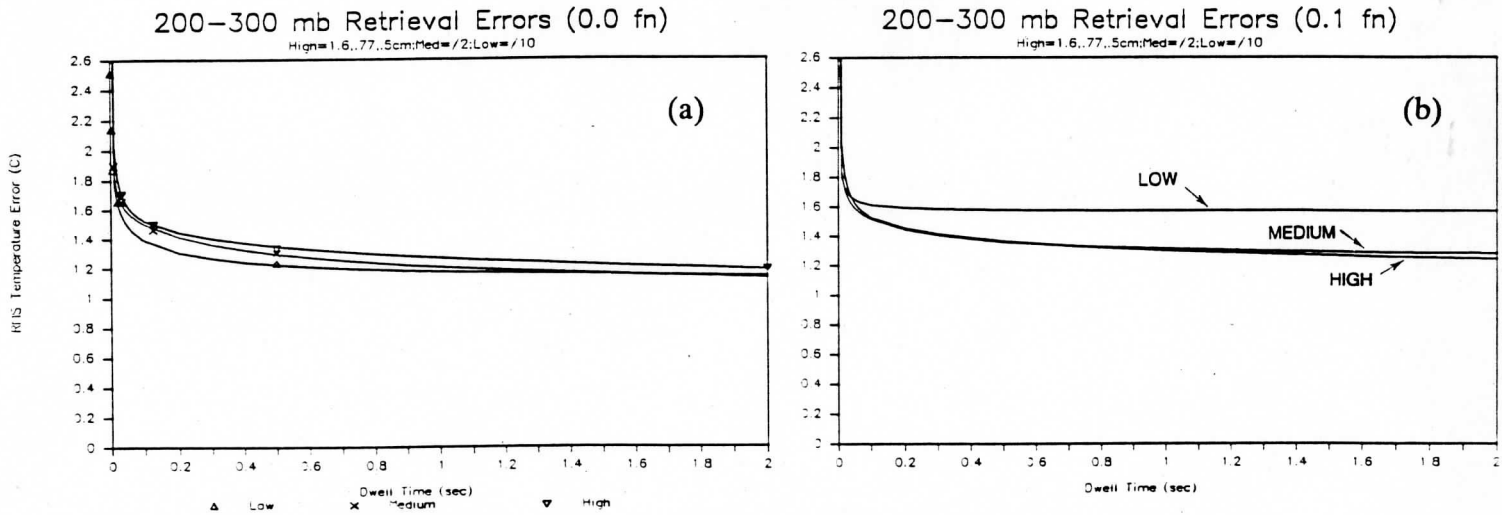

Figure A-4. Retrieval Error vs Dwell Time (a) without and (b) with fixed noise. 200-300mb.

In summary, given the same dwell time both the medium and high resolution modes have a significant performance improvement over that of low resolution mode when "realistic" noise sources are considered. As has been shown in Section 3.2, the advantage of the low resolution mode is its rapid area coverage capability, while the advantage of the high resolution sounding mode is the ability to achieve 1 km vertical resolution in temperature. One can see that the METEOSAT baseline interferometer is an attractive instrument for achieving the desired sounding performance while maintaining high rates of spatial coverage.

APPENDIX B: High-resolution Interferometer Sounder Publications

High-Altitude Aircraft Measurements of Upwelling Radiance (1988)
The Retrieval of Atmospheric Temperature and Water Vapor Profiles (1988)
Radiometric Calibration of IR Fourier Transform Spectrometers (1988)

Mikrochim. Acta [Wien] 1988, II, 439—444

Mikrochimica Acta

High-Altitude Aircraft Measurements of Upwelling IR Radiance: Prelude to FTIR from Geosynchronous Satellite

Henry E. Revercomb[1,*], Daniel D. LaPorte[2], William L. Smith[1], Henry Buijs[3], David G. Murcray[4], Frank J. Murcray[4], and Lawrence A. Sromovsky[1]

[1] Space Science and Engineering Center, University of Wisconsin, 1225 West Dayton Street, Madison, WI 53706, USA
[2] Santa Barbara Research Center, Goleta, CA 93017, USA
[3] Bomem, Vanier, Quebec GiM2Y2, Canada
[4] University of Denver, Denver, CO 80208, USA

Abstract. An aircraft version of the high-resolution interferometer sounder (HIS), a Fourier transform spectrometer designed for meteorological applications, has been used to measure the upwelling infrared emission of the earth with a resolving power on the order of 1000. HIS measurements from high-altitude NASA research aircraft have demonstrated that the high radiometric accuracies required for atmospheric temperature and humidity sounding (1°C absolute brightness temperature and 0.1°C RMS reproducibility) can be achieved. Calibration is accomplished using periodic views of two onboard high-emissivity blackbodies, servo controlled to 300 K and 240 K. For an interferometer, this approach relies on careful optical design and alignment to avoid unknown dependence of the responsivity on optical path difference. The aircraft model is a successful prototype for spacecraft versions for weather and climate monitoring.

Key words: interferometry, spectroscopy, Fourier transform, atmospheric remote sensing, radiometry.

Radiometrically accurate observations of upwelling radiance at 20 km above the earth's surface have been made for meteorological applications from the NASA U-2/ER-2 research aircraft. The objectives are to (1) demonstrate the capability of an interferometer to measure precisely the thermal emission spectrum with a resolving power on the order of 10^3 and (2) provide spectra over varied weather conditions to explore the full

* To whom correspondence should be addressed

potential of high resolution IR data for atmospheric remote sensing. The primary focus is on retrieval of temperature and water vapor profiles with substantially higher vertical resolution and accuracy than is possible from the low spectral resolution measurements of filter radiometer sounding instruments on current weather satellites [1]. A primary goal is the implementation of high spectral resolution instruments on geosynchronous satellites to provide greatly improved meteorological observations for mesoscale forecasting (Joint support was provided by NOAA/NESDIS and NASA) [2]. Valuable information on the radiation budget, minor constituent distributions, and the radiative properties of the land surface and clouds would also be provided.

Instrument Description

The high-resolution interferometer sounder (HIS) for the NASA U-2/ER-2 aircraft views directly downward from inside a pod (about 3 m long and 0.5 m in diameter) mounted either under the wing or under the center line of the fuselage on the ER-2. Operating mode changes for thermal and recorder control are switch-selected by the pilot. Many of the important specific parameters of the design are listed in Table 1.

Calibration is accomplished by viewing two high emissivity blackbodies, servo controlled at altitude to 300 K and about 240 K. After 12 scans of the earth over the full range of optical path, a 45° scene switching mirror rotates the field-of-view from the open earth viewing port to give 4 scans of the hot and 4 scans of the cold blackbodies. The blackbodies, built and calibrated by Eppley Labs, are blackened cavities with thermoelectric cooler/heaters for temperature control and PRT's for monitoring. The temperature of the interferometer optics is not actively controlled.

The Bomem Michelson interferometer [3] as modified for this application provides double sided interferograms from both scan directions. Its auto-alignment system makes it possible to operate in the ambient thermal environment of the pod and in very close proximity to the aircraft jet engine; optical alignment has never been lost. The optical bench is shock mounted to damp high frequency vibration and the interferometer is evacuated to protect the beamsplitter during descent.

The three spectral channels, covering most of the region from 3.8 to 16.6 μm (Table 1), are split inside a single LHe dewar which contains three sets of bandpass cold filters, focussing optics, and arsenic-doped silicon detectors. The preamplifiers are external and operate near the ambient pod temperature of about 260 K. The gain of each channel is fixed and the signals are digitized with a 16 bit A/D. Onboard numerical filtering is used to reduce the sample rate from the HeNe laser rate by factors of 14, 8 and 8 in bands I, II and III.

The data system is controlled with a 6809 microprocessor based system built at the University of Denver. The three channels of interferometer data and housekeeping parameters are combined and recorded on formated cassette tapes. Two drives with a capacity of 67 MBytes each are used to provide 9 h of continuous recording time.

Table 1. Characteristics of the HIS aircraft instrument

Spectral range (cm^{-1})[a]:	
Band I	590—1070
Band II	1040—1930
Band III	2070—2750
Field of view diameter (mr):	
Telescope	100
Interferometer	30
Blackbody reference sources:	
Emissivity	> 0.998
Aperture diameter (cm)	1.5
Temperature stability (K)	± 0.1
Auto-aligned interferometer:	modified Bomem BBDA2.1
Beamsplitter:	
Substrate	KCl
Coatings (¼ λ at 3.3 μm)	Ge + Sb_2S_3
Maximum delay (double sided)-current configuration (cm):	
Band I (hardware limit is ± 2.0)	± 1.8
Bands II and III (limited by data system)	+ 1.2, − 0.8
Michelson mirror optical scan rate (cm/s):	0.6—1.0
Aperture stop (at interferometer exit window):	
Diameter (cm)	4.1
Central obscuration area fraction	0.17
Area (cm^2)	10.8
Area-solid angle product (cm^2-sr):	0.0076
Detectors:	
Type	Ar doped Si
Diameter (cm)	0.16
Temperature (K)	6

[a] The ranges shown are design ranges. The current bandpass filters were chosen from available stock filters, and will be changed as new filters are acquired

Processing of selected data in the field is performed on IBM XT/AT microcomputers. Data is transferred to hard disk and is processed with custom software which displays the measured interferograms and corresponding spectra, and performs calibration to yield radiance or brightness temperature spectra. The calibration procedure uses full complex spectra to avoid errors that can arise from radiance emitted by the warm interferometer [4].

Radiometric Performance

The RMS detector noise for a single 6 s scan determined from in-flight calibration data is shown in Fig. 1. For bands I and II the noise is background limited, with radiation from the instrument providing most of the photons. Band III noise is considerably higher, with a contribution from about 2150—2350 cm^{-1} which is not detector noise.

The other type of noise encountered in flight is sample-position-error noise caused by the effect of aircraft vibrations on the velocity of the

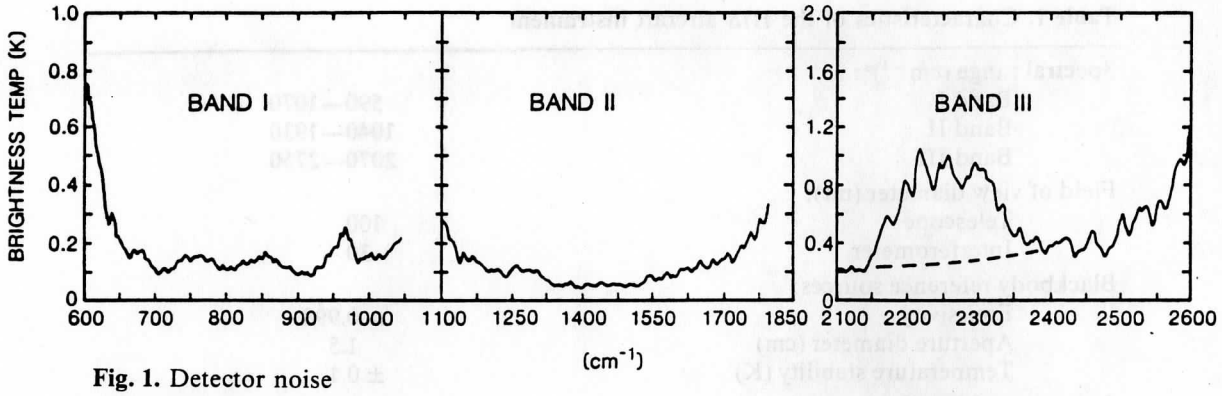

Fig. 1. Detector noise

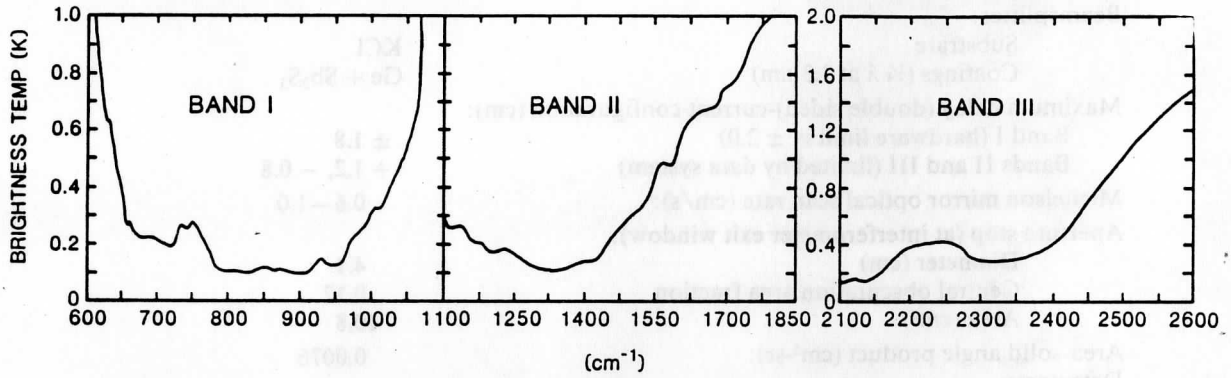

Fig. 2. Sample position error noise for November 2, 1986 ER-2 flight. On the ground, and even in the alternative under-wing configuration, these errors are smaller than detector noise

scanning Michelson mirror. Since it originates from very near ZPD, this noise is highly correlated with wave number, causing a small rocking of the spectra. It is absent on the ground and would not be present in a spacecraft application. Even in the hostile aircraft environment, this noise can be made small as shown in Fig. 2 for operation under the centerline of the ER-2. The amplitude of this noise varies with instrument configuration, and is significantly lower when the HIS is located under the wing.

Accurate radiometric calibration over the full spectral range was demonstrated on the ground using a third blackbody. A liquid nitrogen blackbody was used as the cold reference, one on-board blackbody served as the 300 K hot reference, and the temperature of the other on-board blackbody (set between 260 and 280 K) was determined. The unknown temperature can be determined routinely to within about 0.2 to 0.4 K. This procedure relies on a careful optical design and alignment to prevent OPD dependence of the responsivity, which would degrade the high resolution integrity of the spectra. Self-apodization is kept small by the relatively small field-of-view (FOV) of the interferometer, and can be accounted for accu-

Fig. 3. Brightness temperature spectra from April 14, 1986 flight over the Pacific Ocean near NASA Ames Research Center compared to calculated spectra. The measured spectra are the mean of the spectra from one forward and one backward OPD scan

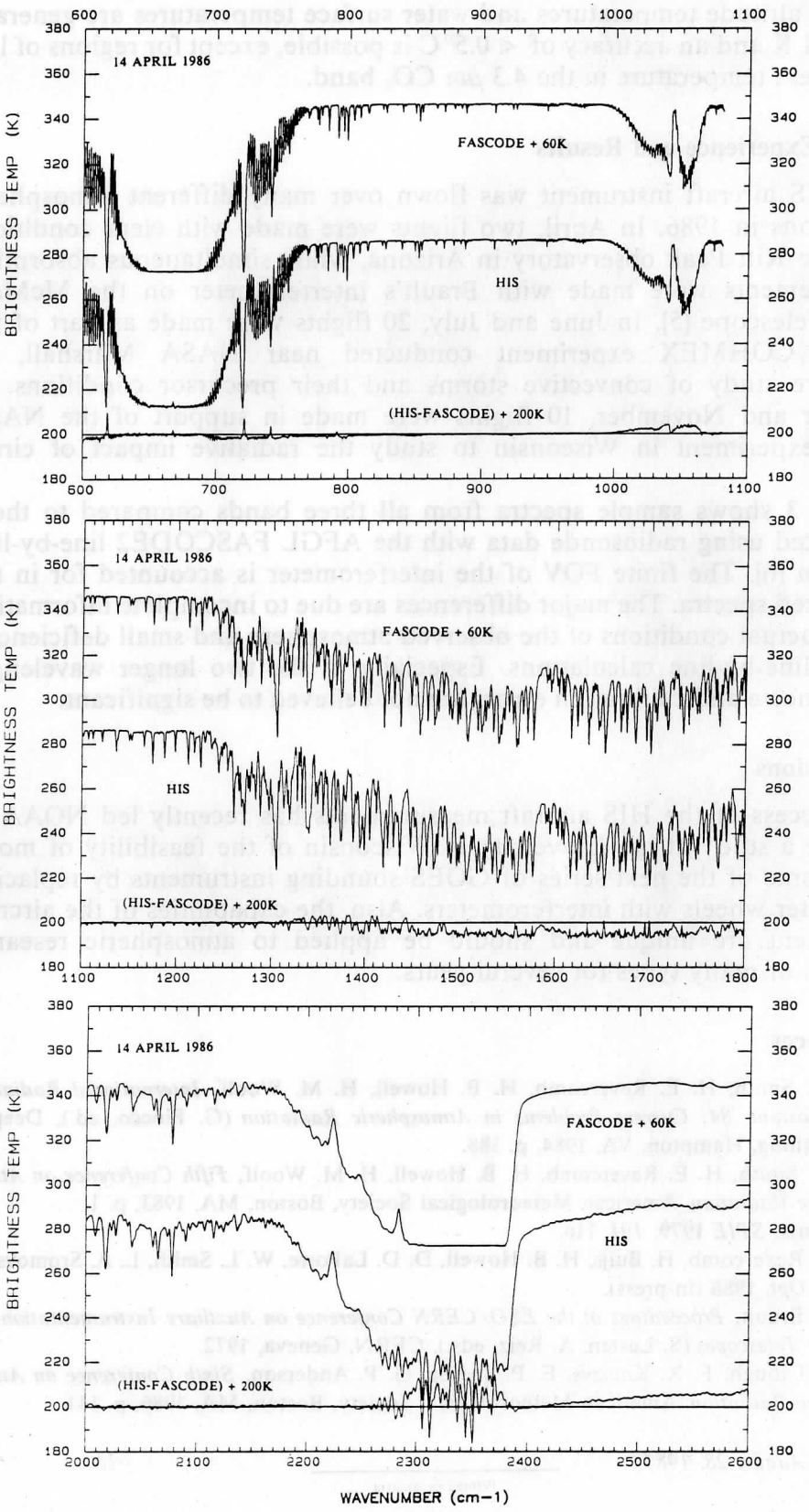
14 APRIL 1986
FASCODE + 60K
HIS
(HIS-FASCODE) + 200K
BRIGHTNESS TEMP (K)
14 APRIL 1986
FASCODE + 60K
HIS
(HIS-FASCODE) + 200K
BRIGHTNESS TEMP (K)
14 APRIL 1986
FASCODE + 60K
HIS
(HIS-FASCODE) + 200K
BRIGHTNESS TEMP (K)
WAVENUMBER (cm−1)

rately. Additional errors could be present in flight, but comparisons with aircraft altitude temperatures and water surface temperatures are generally within 1 K and an accuracy of $< 0.5°C$ is possible, except for regions of low brightness temperature in the 4.3 μm CO_2 band.

Flight Experience and Results

The HIS aircraft instrument was flown over many different atmospheric conditions in 1986. In April, two flights were made with clear conditions over the Kitt Peak observatory in Arizona, while simultaneous absorption measurements were made with Brault's interferometer on the McMath Solar Telescope [5]. In June and July, 20 flights were made as part of the NASA COHMEX experiment conducted near NASA Marshall, an intensive study of convective storms and their precursor conditions. In October and November, 10 flights were made in support of the NASA FIRE experiment in Wisconsin to study the radiative impact of cirrus clouds.

Fig. 3 shows sample spectra from all three bands compared to those calculated using radiosonde data with the AFGL FASCODE2 line-by-line program [6]. The finite FOV of the interferometer is accounted for in the calculated spectra. The major differences are due to incomplete information on the actual conditions of the observed atmosphere and small deficiencies in the line-by-line calculations. Especially in the two longer wavelength bands, noise and calibration errors are not believed to be significant.

Conclusions

The success of the HIS aircraft measurements has recently led NOAA to support a study at the University of Wisconsin of the feasibility of modifying some of the next series of GOES sounding instruments by replacing their filter wheels with interferometers. Also, the capabilities of the aircraft instrument are unique and should be applied to atmospheric research projects of many types for several years.

References

[1] W. L. Smith, H. E. Revercomb, H. B. Howell, H. M. Woolf, *International Radiation Symposium '84: Current Problems in Atmospheric Radiation* (G. Fiocco, ed.), Deepak Publishing, Hampton, VA, 1984, p. 388.

[2] W. L. Smith, H. E. Revercomb, H. B. Howell, H. M. Woolf, *Fifth Conference on Atmospheric Radiation*, American Meteorological Society, Boston, MA, 1983, p. 1.

[3] H. Buijs, *SPIE* **1979**, *191*, 116.

[4] H. E. Revercomb, H. Buijs, H. B. Howell, D. D. LaPorte, W. L. Smith, L. A. Sromovsky, *Appl. Opt.* **1988** (in press).

[5] J. W. Brault, *Proceedings of the ESO/CERN Conference on Auxiliary Instrumentation for Large Telescopes* (S. Lusten, A. Reiz, eds.), CERN, Geneva, 1972.

[6] S. A. Clough, F. X. Kneizys, E. P. Shettle, G. P. Anderson, *Sixth Conference on Atmospheric Radiation*, American Meteorological Society, Boston, MA, 1986, p. 141.

Received August 28, 1987.

Printed in Austria

6.4

Reprinted from the Preprint Volume of the 3rd Conference on Satellite Meteorology and Oceanography, Feb. 1-5, 1988, Anaheim, Calif. Published by the American Meteorological Society, Boston, Mass.

HIGH RESOLUTION INTERFEROMETER SOUNDER - THE RETRIEVAL OF ATMOSPHERIC TEMPERATURE AND WATER VAPOR PROFILES

W. L. Smith[1], H. M. Woolf[2], H. B. Howell[2], H. E. Revercomb[1], and H.-L. Huang[1]

[1]Space Science and Engineering Center
[2]NOAA/NESDIS Systems Design and Applications Branch
Cooperative Institute for Meteorological Satellite Studies
Madison, Wisconsin 53706

1. INTRODUCTION

The High resolution Interferometer Sounder (HIS) is the first of a new generation of passive remote sensors for achieving high vertical resolution sounding information. An aircraft version of HIS is a Michelson Interferometer with a spectral resolving power ($\lambda/\Delta\lambda$) of approximately 2000 covering a spectral range from 3.7-16.7μm. A spacecraft version of the instrument is under development for operational geostationary applications beginning around 1995. In this paper, a technique is described for retrieving atmospheric profiles from the 3000 spectral radiance observations provided by the HIS. Results achieved from spectral radiances observed from the NASA ER2 aircraft are compared with radiosondes and soundings obtained by the VISSR Atmospheric Sounder (VAS) to demonstrate the improved sounding performance achieved with the HIS.

The use of high spectral resolution interferometry will enable the achievement of optimal performance of passive remote sounders. To approach the ultimate limit of vertical resolving power of passive radiometers, the sounding instrument must achieve a spectral resolution better than 0.1%. With this resolution, one avoids smearing contributions to the upwelling radiances from relatively opaque line centers with radiances from much more transparent regions in between the absorption lines.

For examples, Figs. 1 and 2 show the effect of spectral resolution on radiance smearing. The radiance spectrum was achieved with the airborne version of the High resolution Interferometer Sounder (HIS) (Smith et al., 1986) from the NASA U2 aircraft overflying Huntsville, Alabama on June 15, 1986. The HIS spectra are achieved at a resolution of about 0.5 cm^{-1} from 600-1100 cm^{-1} (9.1-16.7μm), and 1.0 cm^{-1} resolution from 1100-2700 cm^{-1} (3.7-9.1μm). The ground resolution and spacing of the HIS observations is 2 km from the U2 altitude of 65,000 feet. The noise equivalent temperature and calibration accuracy are both about 0.1-0.2°C over much of the spectrum (Revercomb et al., 1987). In Fig. 1, blackened portion of the bars representing the half power spectral bandwidths of the current GOES VISSR Atmospheric Sounder, VAS, (Smith et al., 1981) are shown for comparison. In Fig. 2, the brightness temperature spectrum of a small portion of the R-branch of the 15 μm CO_2 band is shown at the HIS resolution and at the nominal 15 cm^{-1} resolution of the filter radiometers such as the VAS. It can be seen that brightness temperature smearing of the order of 30°K occurs as a result of the inability of the filter radiometer to resolve the CO_2 lines which have a typical spacing of 1.7 cm^{-1} (0.03μm) in this spectral region. A 30°K brightness temperature smearing corresponds to a typical vertical temperature gradient over a 5 km depth of the atmosphere. Considering that the width of a monochromatic weighting function is 8 km, the added 5 km smearing due to inadequate spectral resolution causes an additional 60% degradation of vertical resolving power in spectral regions where all the absorption lines are of equal strength. Because the line strengths will vary considerably over a 15 cm^{-1} interval (see Fig. 2), additional vertical resolving power degradation occurs.

Figure 3 shows typical Planck radiance weighting functions for a VAS and HIS spectral channel. One can see that there is a 50 percent greater resolving power in a single HIS channel than in a single VAS channel. The ultimate vertical resolution of atmospheric profiles derived from a set of spectral radiances depends

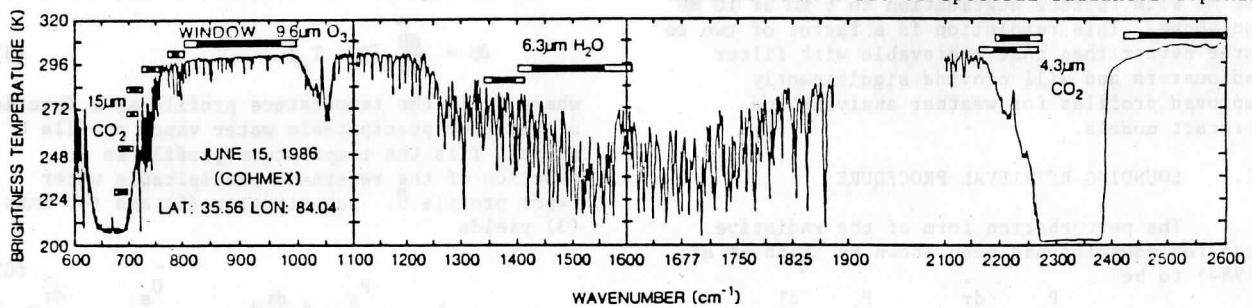

Fig. 1. HIS observed spectrum with VAS spectral bandwidths superimposed.

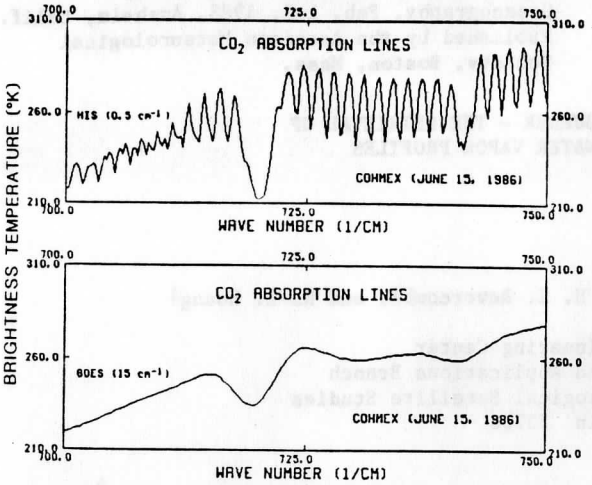

Fig. 2. CO_2 emission spectrum at HIS (0.5 cm^{-1}) resolution (top) and VAS (15.0 cm^{-1}) resolution (bottom).

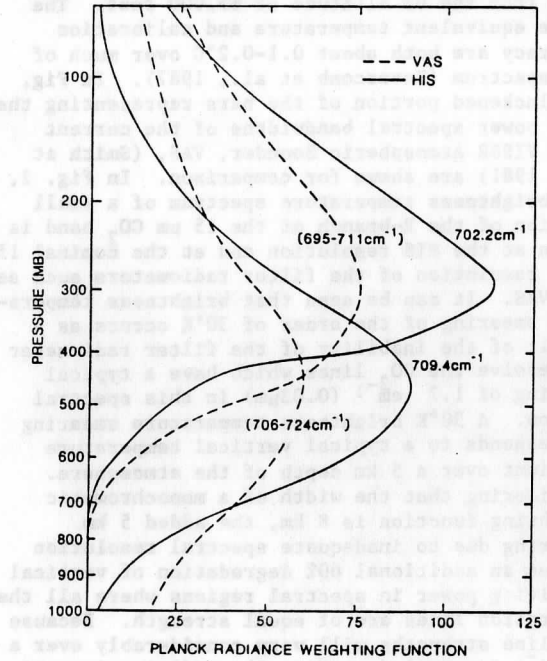

Fig. 3. Plank radiance weighting functions ($d\tau/d\ln p$) at HIS and VAS spectral resolutions.

on the number of spectral channels, their positions, and the noise level of the radiances. The expected vertical resolution of HIS soundings has been determined from theoretical analyses to degrade from 0.7 km near the surface to 3 km at 100 mb with further degradation to 6 km at 10 mb and above. This resolution is a factor of two to three better than that achievable with filter radiometers and will provide significantly improved profiles for weather analysis and forecast models.

2. SOUNDING RETRIEVAL PROCEDURE

The perturbation form of the radiative transfer equation has been shown by Smith et al. (1984) to be

$$\delta T_B = \delta T_s f_s \hat{\tau}_s - \int_o^{P_s} \delta T f \frac{d\hat{\tau}}{dp}\, dp + \int_o^{P_s} \delta\tau f \frac{dT}{dp}\, dp \quad (1)$$

where δT_B is the deviation of the observed brightness temperature, T_B, for a given wavelength, from that corresponding to a reference or guess atmospheric temperature and water vapor profile condition, δT_s is the deviation of the actual surface skin temperature from the reference condition, δT is the deviation of the true atmospheric temperature, T, from its reference, T, $\delta\tau$ is the deviation of the true spectral transmittance profile from that corresponding to the reference water vapor profile condition, $\hat{\tau}$, and f is the ratio $(\partial B/\partial T_B)/(\partial B/\partial T)$ where B is Planck radiance.

With the HIS, we have 3000 spectral channels sensitive to the surface temperature and the temperature and water vapor profile. The sensitivity of the radiances to temperature and water vapor varies greatly across the spectrum due to the degree of overlap between water vapor absorption lines and lines due to uniformly mixed gases such as CO_2 and N_2O. Also, the Planck function dependence upon wavelength and temperature contributes to the spectrally varying sensitivity. Because of the mutual dependence of radiance on temperature and water vapor, it is desirable to solve for the temperature and water vapor profile simultaneously from the complete set of spectral observations. A simultaneous solution is achieved by noting that for the very high HIS spectral resolution, the atmospheric transmittance can be represented as the product of those for water vapor and dry air. Thus,

$$\hat{\tau} = \tau_d \hat{\tau}_w \quad (2)$$

In (2), τ_d is the transmittance of the "dry" atmosphere which is a function of the uniformly mixed gases whose concentrations are known and τ_w is the spectral transmittance due to water vapor alone. (Ozone is included in τ_d.) Using (2) in (1) yields

$$\delta T_B = f_s \delta T_s \hat{\tau}_s - \int_0^{P_s} f \delta T\, \hat{\tau}_w \frac{d\tau_d}{dp} dp$$

$$- \int_0^{P_s} f \delta T\, \tau_d \frac{d\hat{\tau}_w}{dp} dp + \int_0^{P_s} f \tau_d \delta\tau \frac{dT}{wdp} dp \quad (3)$$

In order to solve (3) for the water vapor profile, let

$$\delta\tau_w \cong \frac{d\hat{\tau}_w}{d\hat{U}} \delta U \quad (4)$$

where U is the precipitable water vapor profile. Furthermore we note that

$$\delta U = \frac{d\hat{U}}{dT} (T - T_w) \quad (5)$$

where T_w is the temperature profile as a function of the true precipitable water vapor profile U whereas T is the temperature profile as a function of the reference precipitable water vapor profile $\hat{U}$. Substituting (5) and (4) into (3) yields

$$\delta T_B = f_s \delta T_s \hat{\tau}_s - \int_0^{P_s} f \delta T \hat{\tau}_w \frac{d\tau_d}{dp} dp - \int_0^{\hat{U}_s} f \delta T_w \tau_d \frac{d\hat{\tau}_w}{d\hat{U}} d\hat{U} \quad (6)$$

where $\delta T = T - \hat{T}$ and $\delta T_w = T_w - \hat{T}$. Equation (6) describes the perturbation of the observed brightness temperature spectrum from a reference condition in terms of three variables: the deviation of the true surface skin temperature from the reference, the deviation of the atmospheric temperature profile from the reference profile as a function of pressure and the deviation of the atmospheric temperature profile from the reference profile as a function of atmospheric precipitable water vapor content. Note that if the reference precipitable water vapor concentration as a function of pressure is correct then $\tau_w = \tau_w$, $\delta T_w = \delta T$ so that the two integrals combine to yield the normal form of the radiative transfer equation ($f\delta T\tau_s - \int_0^{P_s} f\delta T(d\tau/dp)dp$). Otherwise, $\delta T_w \neq \delta T$ so that the T and T_w profiles resulting from the solution of (6) will differ from each other depending upon the error in the presumed water vapor condition.

The numerical solution of (6) is achieved by using a basis function representation of δT and δT_w; namely,

$$\begin{matrix} \delta T(p) \\ \text{and} \\ \delta T_w(p) \end{matrix} = \sum_{i=1}^{N} C_i \phi_i(p) \qquad (7)$$

where $\phi_i(p) = (p/p_i^*)\,\mathrm{Exp}(-p/p_i^*)$ where p is atmospheric pressure and p_i^* is the pressure of the "standard" atmospheric pressure levels (1000, 850, 700, 500, 400, 300, 250, 200, 150, 100, 70, 50 mb). The functions $\phi_i(p)$ can be shown to be equivalent to Planck radiance weighting functions ($d\tau/d\ln p$) of a uniformly mixed absorbing constituent peaking at the pressure p_i^*. Substituting (7) into (6) gives the system of equations

$$\delta T_{Bj} = \sum_{i=0}^{M} C_i A_{ij} \qquad j = 1, 2,,,K \qquad (8)$$

where K is the number of spectral channels and

$$C_0 = \delta T_s \,, \quad A_0 = f_{sj}\hat{\tau}_{sj}$$

$$A_{ij} = \int_0^{P_s} \phi_i(p) f_j \hat{\tau}_{wj}(p) d\tau_{dj}(p) \qquad i = 1, 2,,,M/2$$

$$A_{ij} = \int_0^{P_s} \phi_i(p) f_j \hat{\tau}_{dj}(p) d\hat{\tau}_{wj}(p) \qquad i = \frac{M}{2} + 1, \frac{M}{2} + 2,,,M$$

where M/2 is the number of "standard" atmospheric pressure levels. In the case of the aircraft HIS experiment, K is approximately 2500 and M is 24. Thus, (8) represents a system of 2500 equations with 25 unknowns.

The solution of (8) is achieved using the conditioned least squares inverse solution

$$\vec{C} = (A^T A + \gamma I)^{-1} A^T \vec{t}_b = A^* \vec{t} \qquad (9)$$

where $\vec{t}$ is the vector of brightness temperature observations (δT_B), A^* is the solution matrix, I is the identity matrix, and γ is a Lagrangian multiplier ($=10^{-2}$) used to condition the matrix $A^T A$ for inversion. The superscript T denotes matrix transposition.

When utilizing brightness temperature observations it is proper to account for the errors in δT_B due to measurement errors and to uncertainties in the atmospheric transmittance observations used to calculate $\hat{T}_B$ from $\hat{\tau}(p)$ and U(p). This error can be defined as

$$\varepsilon_j = \sqrt{\rho_j^2 + \eta_j^2} \qquad (10)$$

where $\rho = r/(\partial B/\partial T_B)$ is the expected random brightness temperature measurement error (r_j being the radiance error) specified from the observations when viewing a constant calibration source, and η_j is the difference between the observed and calculated brightness temperature for known atmospheric conditions. In order to account for the spectral dependence of ε_j, both sides of equation (8) are scaled by ε_j (i.e., $\delta T_{Bj} = \delta T_{Bj}/\varepsilon_j$ and $A_{ij} = A_{ij}/\varepsilon_j$). Thus, the spectral regions whose observation error and atmospheric transmittance uncertainties are smallest carry the greatest weight in the solution for the atmospheric profiles.

Having determined the coefficient vector $\vec{C}$, the atmospheric profiles T(p) and $T_w(p)$ are obtained from (7). The water vapor concentration profile U(p) is then obtained using (5) in the form

$$U(p) = \hat{U}(p) + \frac{d\hat{U}(p)}{dT(p)} [T(p) - T_w(p)] \qquad (11)$$

or

$$U(p) = \hat{U}(p) \left[1 + \frac{T(p) - T_w(p)}{d\hat{T}/d\ln\hat{U}}\right] \qquad (12)$$

The mixing ratio profile is then calculated using the relation

$$q(p) = \hat{q}(p) \frac{dU(p)/dp}{d\hat{U}(p)/dp} = \hat{g}(p) \frac{dU(p)}{d\hat{U}(p)} \qquad (13)$$

where all the vertical derivations are computed as centered finite differences.

3. ATMOSPHERIC TRANSMITTANCES AND CALCULATED RADIANCE SPECTRA

The atmospheric transmittance functions for water vapor, $\tau_w(p)$, and $\tau_d(p)$ are calculated using the line-by-line transmittance model "FASCODE" (Clough et al., 1986). For the calculation of the radiance corresponding to the reference sounding condition, the total transmittance is calculated considering all optically active constituents (H_2O, CO_2, N_2O, CH_4, $O3$, N_2, SO_2, NO, CO, etc.) simultaneously. In order to represent the HIS spectra, the transmittances are calculated at high spectral resolution ($\sim$0.06 cm^{-1}) and then transformed to an interferogram incorporating the spectral response and finite field of view properties of the airborne HIS instrument. The interferogram is

$$\tau_x(p) = \int_0^\infty \tau_\nu(p)\phi_\nu \frac{\sin 2\pi\nu x\alpha^2/4}{2\pi\nu x\alpha^2/4} \cos(2\pi\nu x)d\nu \quad (14)$$

where x is delay, $\tau_\nu(p)$ is the spectral transmittance as a function of wavenumber, ν, α is the half angle field of view of the HIS and ϕ_ν is the spectral response function due primarily to the interference filter used to limit the incoming radiation. Then $\tau_\nu(p)$ for the HIS resolution is achieved using a cosine transform of $\tau_x(p)$ using precisely the same delay cutoff and interferogram apodization function used to process the HIS interferogram radiance observations.

$$\tau_\nu(p) = 2\int_0^{X_m} \tau_x(p)\Psi_x \cos(2\pi\nu x)dx \quad (15)$$

where X_m=1.4 for band 1 (600-1100 cm^{-1}), X_m=0.9 for band 2 (1100-1900 cm^{-1}), and band 3 (2000-2700 cm^{-1}). In the processing of the HIS spectra, the apodization is

$$\Psi_x = (1 - x^2/X_m^2)^2 \quad (16)$$

Figure 4 shows spectra of radiance computed from the average of two special radiosonde observations taken at 17 GMT near Huntsville, Alabama on June 15, 1986. The radiosonde observations were taken in support of the COoperative Huntsville Meteorological EXperiment (COHMEX) to study convective weather. Also shown is an average of HIS spectra observed in the vicinity of the two radiosonde observations. The differences generally exceed the single sample observation errors of 0.2 mw/m^2-cm^{-1}-sr for band 1, 0.1 mw/m^2-cm^{-1}-sr for band 2, and 0.01 mw/m^2-cm^{-1}-sr for band 3. These differences are due to errors in simulating the spectral characteristics of the HIS observations in the radiance computations, errors in the radiosonde observations, errors in the FASCODE transmittance computations, and errors due to quadrature in the radiative transfer computations. These discrepancies are accounted for in the retrieval algorithm through their inclusion in the estimation of the forward radiance computation error spectrum defined by Eq. (10). Furthermore, we attempt to correct the calculated spectra for their discrepancy with observations using the approximation

$$\hat{T}_B{}^c(\nu) = \hat{T}_B(\nu) + \eta(\nu) \quad (17)$$

where $\hat{T}_B{}^c(\nu)$ is the corrected radiative transfer computation of the brightness temperature spectrum and $\eta(\nu)$ is an expected difference between observed and calculated brightness temperature spectra for known atmospheric conditions as previously defined by Eq. (10).

4. AN EXAMPLE OF ATMOSPHERIC PROFILE RETRIEVALS FROM AIRBORNE HIS SPECTRA

On June 15, 1986, the HIS flew aboard the NASA U2 from Wallops Island, Virginia to the COHMEX observation area over northern Alabama and Tennessee. Figure 5 shows the flight track of the U2 over a GOES visible channel cloud image at 18 GMT, the central time of the U2 flight. As can be seen, the COHMEX area was covered with low

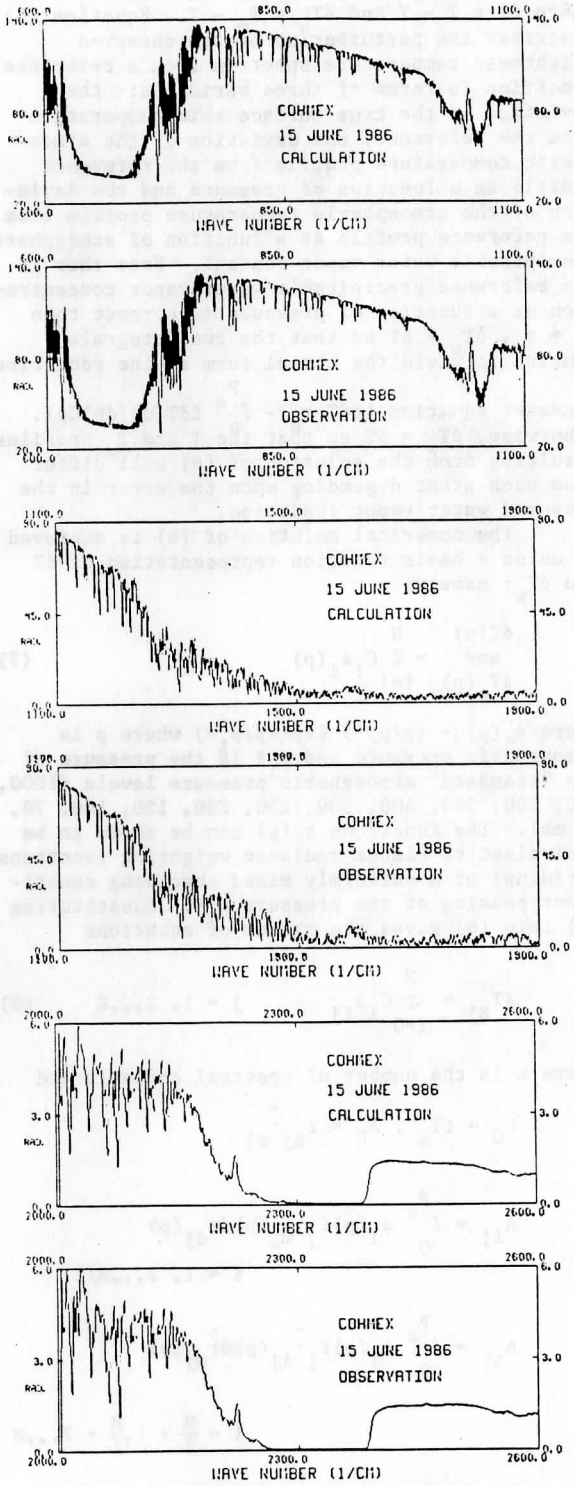

Fig. 4. Calculated and observed radiance for COHMEX region on June 15, 1986.

scattered cumulus clouds whose tops are estimated from radiosonde and HIS window channel brightness temperature data to be at a pressure altitude of 850 mb. In these initial retrievals conducted from the HIS data, no attempt was made to account for the cloud effects on the HIS spectra (i.e., all spectra were handled as if they were observed for cloud-free sky conditions). An NMC forecast temperature and water vapor profile for Huntsville, Alabama was used as the guess profile for all the retrievals to be shown (i.e., the solu-

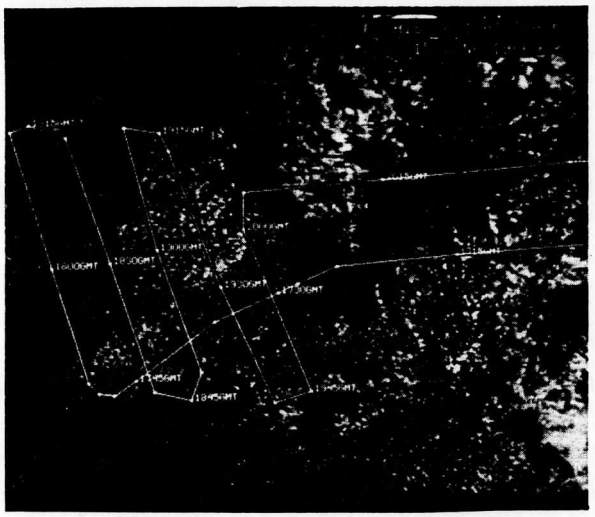

Fig. 5. Flight track of the NASA U2 aircraft overlaying a GOES visible image.

tion matrix, A* of Eq. (9), was computed once and held constant for all the retrievals).

Figure 6 shows a plot of HIS retrieved dewpoint at 300 mb overlaying a VAS 6.7μm water vapor image. Also shown are the few special radiosonde observations conducted in this area. As can be seen, there is a systematic difference between the HIS and radiosonde dewpoints at 300 mb, the radiosonde being warmer by 4.0°C. However, the horizontal gradient is in excellent agreement (i.e., within 1°C). Also, there is excellent agreement between the small scale horizontal features of the retrieved dewpoints and the moisture gradients revealed in the VAS moisture channel image.

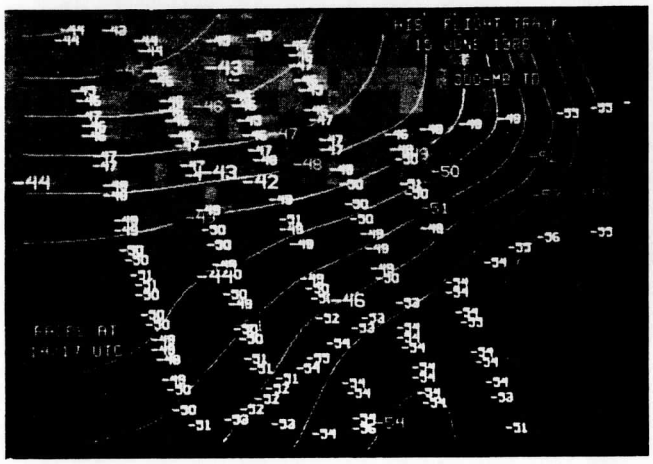

Fig. 6. HIS 300 mb dewpoint temperatures observed along the U2 flight track. The image is from the VAS 6.7μm water vapor channel. Dark regions correspond to high radiance (i.e., low values of water vapor concentration). Radiosonde values are shown as the large numbers.

Figure 7 shows an example skew T-log P diagram comparing a HIS profile retrieval with a radiosonde and the NMC guess, and VAS profile retrieval with the same radiosonde. The NMC first guess profile was used for both the HIS and VAS profile retrieval. The ability of the HIS to resolve the fine scale vertical structure of atmospheric moisture, in particular, is remark-

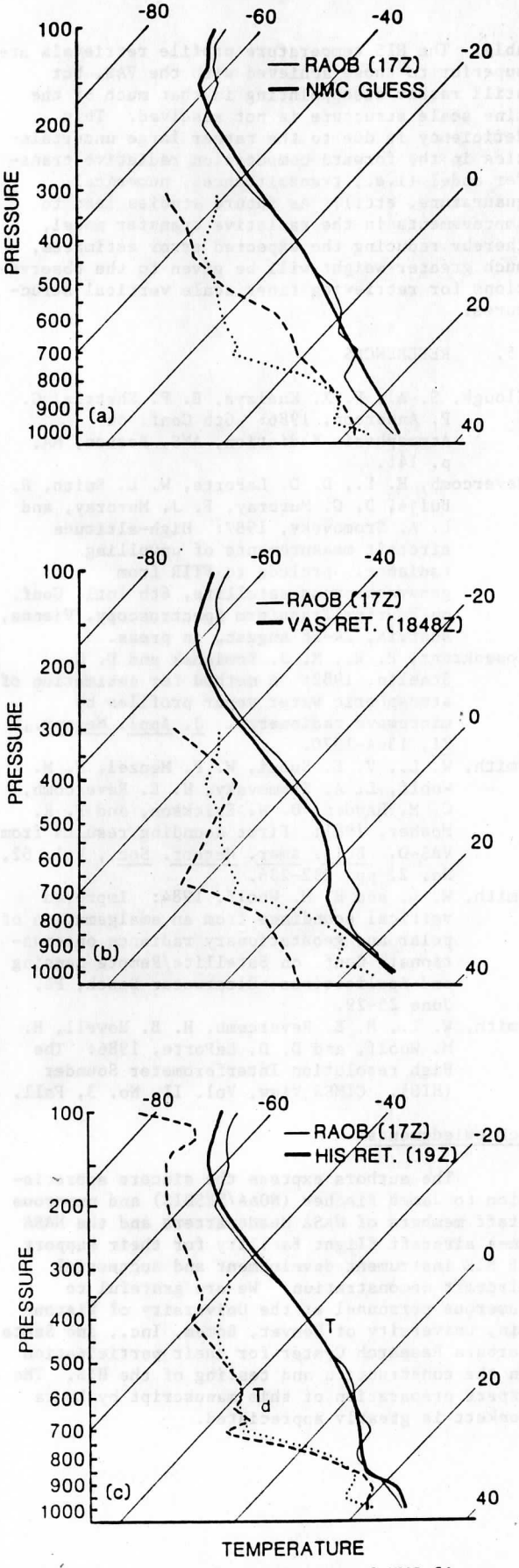

Fig. 7. An example comparison of NMC first guess, VAS retrieval, and HIS retrieval with a nearly coincident radiosonde observation.

able. The HIS temperature profile retrievals are superior to those achieved with the VAS, but still rather disappointing in that much of the fine scale structure is not resolved. This deficiency is due to the rather large uncertainties in the forward computation radiative transfer model (i.e., transmittances, numerical quadrature, etc.). As future studies lead to improvements in the radiative transfer model, thereby reducing the expected error estimates, much greater weight will be given to the observations for retrieving finer scale vertical structures.

5. REFERENCES

Clough, S. A., F. X. Kneizys, E. P. Shettle, G. P. Anderson, 1986: 6th Conf. on Atmospheric Radiation, AMS, Boston, MA, p. 141.

Revercomb, H. E., D. D. LaPorte, W. L. Smith, H. Buijs, D. G. Murcray, F. J. Murcray, and L. A. Sromovsky, 1987: High-altitude aircraft measurements of upwelling radiance: prelude to FTIR from geosynchronous satellite, 6th Intl. Conf. on Fourier Transform Spectroscopy, Vienna, Austria, 24-28 August, in press.

Rosenkranz, P. W., M. J. Komichak and D. H. Staelin, 1982: A method for estimation of atmospheric water vapor profiles by microwave radiometry. J. Appl. Meteor., 21, 1364-1370.

Smith, W. L., V. E. Suomi, W. P. Menzel, H. M. Woolf, L. A. Sromovsky, H. E. Revercomb, C. M. Hayden, D. N. Erickson, and F. R. Mosher, 1981: First sounding results from VAS-D. Bull. Amer. Meteor. Soc., Vol. 62, No. 2, pp. 232-236.

Smith, W. L. and H. M. Woolf, 1984: Improved vertical soundings from an amalgamation of polar and geostationary radiance observations. Conf. on Satellite/Remote Sensing and Applications, Clearwater Beach, FL, June 25-29.

Smith, W. L., H. E. Revercomb, H. B. Howell, H. M. Woolf, and D. D. LaPorte, 1986: The High resolution Interferometer Sounder (HIS). CIMSS View, Vol. II, No. 3, Fall.

Acknowledgments

The authors express the sincere appreciation to James Fischer (NOAA/NESDIS) and numerous staff members of NASA Headquarters and the NASA Ames aircraft flight facility for their support of HIS instrument development and successful aircraft demonstration. We are grateful to numerous personnel at the University of Wisconsin, University of Denver, Bomem, Inc., and Santa Barbara Research Center for their participation in the construction and testing of the HIS. The expert preparation of this manuscript by Laura Beckett is greatly appreciated.

Reprinted from Applied Optics, Vol. 27 page 3210, August 1, 1988

Radiometric calibration of IR Fourier transform spectrometers: solution to a problem with the High-Resolution Interferometer Sounder

Henry E. Revercomb, H. Buijs, Hugh B. Howell, D. D. LaPorte, William L. Smith, and L. A. Sromovsky

A calibrated Fourier transform spectrometer, known as the High-Resolution Interferometer Sounder (HIS), has been flown on the NASA U-2 research aircraft to measure the infrared emission spectrum of the earth. The primary use—atmospheric temperature and humidity sounding—requires high radiometric precision and accuracy (of the order of 0.1 and 1°C, respectively). To meet these requirements, the HIS instrument performs inflight radiometric calibration, using observations of hot and cold blackbody reference sources as the basis for two-point calibrations at each wavenumber. Initially, laboratory tests revealed a calibration problem with brightness temperature errors as large as 15°C between 600 and 900 cm^{-1}. The symptom of the problem, which occurred in one of the three spectral bands of HIS, was a source-dependent phase response. Minor changes to the calibration equations completely eliminated the anomalous errors. The new analysis properly accounts for the situation in which the phase response for radiance from the instrument itself differs from that for radiance from an external source. The mechanism responsible for the dual phase response of the HIS instrument is identified as emission from the interferometer beam splitter.

I. Introduction

The capability of measuring absolute radiance with an infrared Fourier transform spectrometer is important to the High-Resolution Interferometer Sounder (HIS) program,[1,2] which is applying interferometry to measure the upwelling emission spectrum of the earth for retrieving the temperature, humidity, and other parameters of the atmosphere and surface. The primary objective of the HIS program is to improve significantly the vertical resolution of temperature and humidity profiles determined from satellite platforms by increasing the spectral resolution of observed radiances. The interferometer is a natural choice for the job. Interferometers have proved their merit in space with successful measurements of the emission spectra of planetary atmospheres, not only of the earth,[3,4] but also of Venus,[5] Mars,[6] Jupiter, Saturn and Uranus.[7]

H. Buijs is with BOMEM, Inc., 625 Marais, Ville de Vanier, Quebec G1M 2Y2, Canada; H. B. Howell is with NOAA/NESDIS Systems Design & Applications Branch, 1225 West Dayton Street, Madison, Wisconsin 53706; D. D. LaPorte is with Santa Barbara Research Center, 75 Coromar Drive, Goleta, California 93117; and the other authors are with University of Wisconsin, Space Science & Engineering Center, 1225 West Dayton Street, Madison, Wisconsin 53706.

Received 19 December 1987.

The multiplex and throughput advantages of the interferometer[8] make it possible to make radiometrically precise observations at a much higher spectral resolution than that of current filter radiometers (tens of cm^{-1}). To improve the vertical resolution in the troposphere and lower stratosphere by at least a factor of 2 over that of current temperature profiling radiometers (3–8 km), a resolving power ($\lambda/\Delta\lambda$) of ~1000 is needed in the spectral range from 3.7 to 17 μm. (The 15-μm CO_2 absorption band is the primary band for temperature sounding, the combined 4.3-μm CO_2 and 4.5-μm N_2O bands are used to enhance the temperature resolution in the lower troposphere, and the 6.7-μm H_2O absorption band gives humidity soundings.) High radiometric precision is required because radiometric noise and time-dependent and wavelength-dependent calibration errors are magnified in the inversion process to derive atmospheric parameters. To obtain temperature profiles with rms errors of <1°C from high-resolution measurements requires noise-equivalent-temperature errors and calibration reproducibilities of the order of 0.1°C and absolute errors of less than about 1°C.

Several important steps have been taken toward developing an improved temperature and humidity sounding satellite instrument. The feasibility of building an instrument to achieve the radiometric performance needed from a geosynchronous satellite plat-

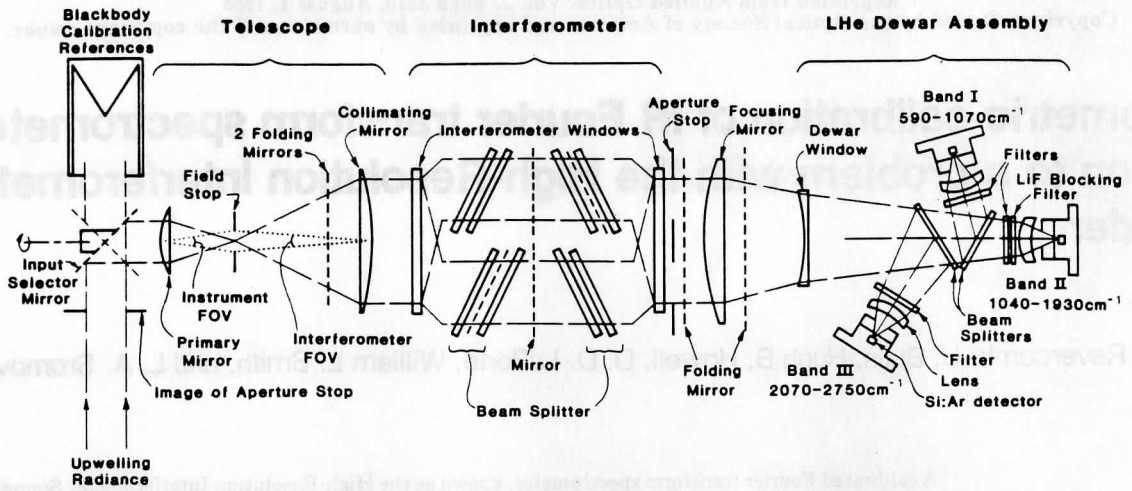

Fig. 1. Functional schematic of HIS optics. The primary mirror, collimating mirror, and focusing mirrors are shown as lenses to simplify the drawing. Plane reflecting surfaces are shown as dashed lines, and the two paths of the interferometer are functionally represented. The complete instrument is ~2.7 m (9 ft) long and fits into the 45.7-cm (18-in.) diam wing pods of the NASA U-2 aircraft.

form has been demonstrated.[9] An aircraft model HIS has been developed and flown on dozens of flights of the NASA U-2 research aircraft as a direct demonstration of the scientific value of such an instrument[10] and that the radiometric noise and calibration requirements are achievable.[11] The instrument was flown with many other atmospheric sensing instruments in two major NASA field programs, the combined Huntsville Meteorological Experiment (COHMEX) for studying severe storms and the First ISCCP Regional Experiment (FIRE) for studying the effect of cirrus clouds on climate. The unique ability of this instrument to measure accurately the emission spectrum from a flexible high-altitude platform with a large complement of other instrumentation should make it an important resource for many types of experiment for several years. Currently, plans for modifying the newest NOAA geosynchronous sounding instrument to incorporate an interferometer are being investigated to realize improvements in the satellite sounding data for weather forecasting before the next century.

This paper describes information about the radiometric calibration of the HIS aircraft instrument, which may be useful to other IR interferometer applications. Early laboratory testing of the aircraft instrument revealed that wavelength-dependent calibration errors of up to 15°C occurred between 600 and 900 cm^{-1} when blackbodies at 300 and 77 K were used to determine the radiance of a 280 K blackbody from the magnitude spectra of each source (Sec. II). These large errors, which were originally believed to require hardware changes to the instrument, have been completely eliminated by the processing technique described in Sec. III. The instrument characteristic responsible for the initial calibration errors is also identified there. The implications of the new calibration analysis technique for interferometer design and performance are summarized in the final section.

II. HIS Radiometric Calibration and the Problem

A. Calibration Approach and Laboratory Test Results

The basic approach for determining absolute radiances from the HIS nadir-viewing interferometer is the same as that used for filter radiometers and has been used successfully for other interferometric applications.[3–7,12] The detectors and electronics are designed to yield an output which is linear in the incident radiance for all wavenumbers in the optical passband of the instrument, and two blackbody reference sources are viewed to determine the slope and offset which define the linear instrument response at each wavenumber.

In the HIS U-2 instrument, calibration observations of the two onboard reference blackbodies are made every 2 min. There are four double-sided optical-path scans of each reference source for every twelve scans of the earth. As shown in Fig. 1, which summarizes the optical configuration, the blackbodies are viewed by rotating the telescope field of view (FOV) from below the aircraft to inside a blackbody aperture using a 45° plane mirror. There are no uncalibrated optical surfaces, since the earth is viewed through an open aperture in the pod, which provides an aerodynamic shell.

The small size of the optical beam at the blackbody positions makes the design of accurate radiation standards relatively easy. The reference blackbodies are thermoelectrically controlled blackened copper cavities. The insulated copper walls of the blackbody cavities give good temperature uniformity, and because of the cavity effect, the normal emissivity is very close to one (Table I). The temperatures are sensed with accurately calibrated platinum resistance thermometers (PRTs) embedded in the base of each cavity. (During testing, a second PRT in the side of the cavity was used to verify adequate temperature uniformity.)

Table I. Characteristics of the HIS Aircraft Instrument

Spectral range (cm^{-1})[a]	
Band I	590–1070
Band II	1040–1930
Band III	2070–2750
Field of view diameter (mrad)	
Telescope	100
Interferometer	30
Blackbody reference sources	
Emissivity	>0.998
Aperture diameter (cm)	1.5
Temperature stability (K)	±0.1
Temperatures (K)	240, 300
Autoaligned interferometer:	Modified BOMEM BBDA2.1
Beam splitter	
Substrate	KCl
Coatings (¼ λ at 3.3 μm)	Ge + Sb_2S_3
Maximum delay (double-sided current configuration (cm)	
Band I (hardware limit is ±2.0)	±1.8
Bands II and III (limited by data system)	+1.2, −0.8
Michelson mirror optical scan rate (cm/s)	0.6–1.0
Aperture stop (at interferometer exit window)	
Diameter (cm)	4.1
Central obscuration area fraction	0.17
Area (cm^2)	10.8
Area-solid angle product (cm^2 sr)	0.0076
Detectors	
Type	Ar-doped Si
Diameter (cm)	0.16
Temperature (K)	6
Nominal instrument temperature (K)	260

[a] The ranges shown are design ranges. The current bandpass filters were chosen from available stock filters and will be changed as new filters are acquired.

One important additional requirement when applying a two-point calibration with blackbody references to an interferometer, as opposed to an instrument measuring spectra directly, is that the instrument responsivity should be independent of optical delay (or that any delay dependences should be accurately known). Avoiding sources of delay-dependent response was a major objective in designing the HIS instrument. To accomplish this, care was taken in the optical stop design and alignment to prevent the effective aperture stop size from changing with the motion of the Michelson mirror. The best location for the aperture stop, which is focused on the detectors, was found to be at the exit window of the interferometer module (see Fig. 1). Furthermore, the FOV of the interferometer is restricted to 30 mrad to limit self-apodization.

Now we turn to the mathematical expressions for the calibration. First, a formalism which leads to the use of magnitude spectra in the expression for calibrated radiance is presented to show where this commonly used approach can create a problem, as occurred with the early (1985) HIS calibrations. Assuming linearity as expressed above, the output interferogram F can be expressed in terms of the incident spectral radiance L_ν as follows, using a continuous representation:

$$F(x) = \frac{1}{2}\int_{-\infty}^{\infty} C_\nu \exp[i\phi(\nu)] \exp(i2\pi\nu x)d\nu, \quad (1)$$

where the uncalibrated magnitude spectrum ($C_\nu \equiv C_{-\nu}$) is given by

$$C_\nu = |\tilde{F}| = r_\nu(L_\nu + L_\nu^0), \quad (2)$$

and where x = optical path difference (delay),
ν = wavenumber,
$\phi(\nu)$ = phase response of instrument [$\phi(\nu) = \phi(-\nu)$],
r_ν = responsivity of instrument,
L_ν^0 = offset from instrument emission, referred to input,
$\sim$ = complex Fourier transform.

The phase characterizes the combined optical and electrical dispersion of the instrument and here is assumed to be the same for scene and background emissions. Although this assumption is commonly made, it will later be shown to be invalid for the HIS instrument. Equation (2) expresses the linear relationship between the uncalibrated spectrum and spectral radiance. The two unknowns to be determined from the two calibration observations are the responsivity and the offset radiance. The offset radiance defined here is the radiance, which, if introduced at the input of the instrument, would give the same contribution as the actual emission from various parts of the optical train. Equation (2) written for both the hot and cold blackbody views can be solved to yield

$$r_\nu = (C_{h\nu} - C_{c\nu})/[B_\nu(T_h) - B_\nu(T_c)], \quad (3)$$

$$L_\nu^0 = C_{h\nu}/r_\nu - B_\nu(T_h) = C_{c\nu}/r_\nu - B_\nu(T_c), \quad (4)$$

where B_ν is the Planck blackbody radiance, and subscripts h and c label the quantities associated with the hot and cold blackbody. [Note that for simplicity the blackbodies are assumed to have unit emittance here. To account for actual emittances ϵ, the Planck radiances should be replaced with $\epsilon B + (1 - \epsilon)B(T_a)$, where T_a is the ambient temperature.] Solving Eq. (2) for the source radiance and substituting from Eqs. (3) and (4) yield the basic calibration relationships:

$$L_\nu = C_\nu/r_\nu - L_\nu^0; \quad (5)$$

$$L_\nu = [(C_\nu - C_{c\nu})/(C_{h\nu} - C_{c\nu})][B_\nu(T_h) - B_\nu(T_c)] + B_\nu(T_c). \quad (6)$$

The ground calibration tests to be reported here consisted of measuring the radiance from a blackbody at ~280 K using calibration blackbodies at 300 and 77 K. The uncalibrated spectra are shown for two of the three HIS spectral bands in Figs. 2 and 3 (see Table I for the nominal spectral coverage of each band). These bands were chosen because band I displays the problem to be discussed here, and band II does not. (Band III also does not.) Both the magnitude and phase are determined directly from a complex Fourier transformation of the measured two-sided interferogram. As will be explained further in Sec. III, the

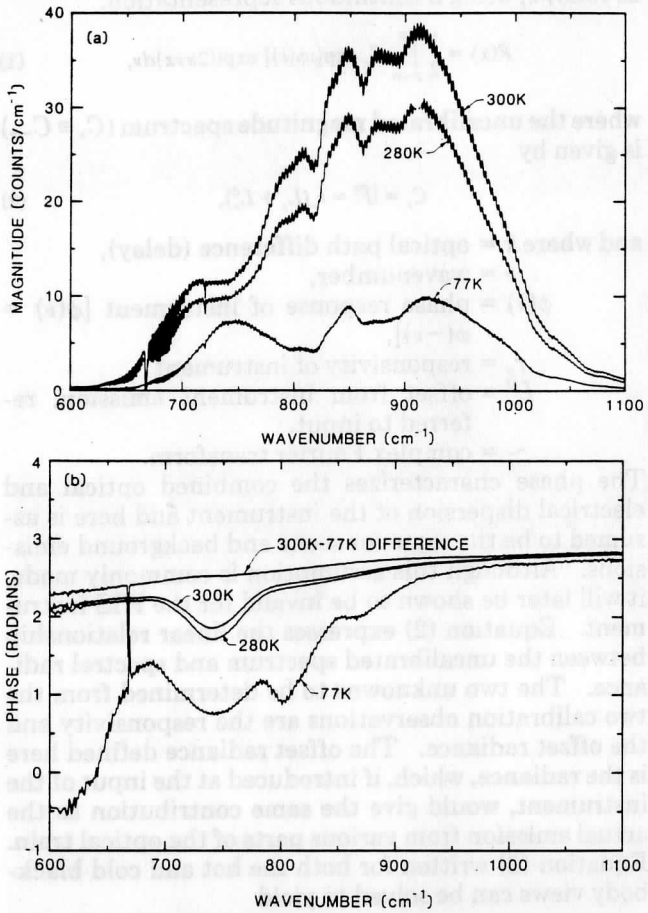

Fig. 2. Uncalibrated magnitude (a) and phase (b) spectra of blackbody sources for HIS spectral band I. The curves are labeled by the temperature of the source. The phase labeled 300K–77K Difference is the phase of the difference of the 300 and the 77 K spectra. The magnitude spectra are shaped by a Gaussian numerical filter and display CO_2 absorption features and channeling as discussed in the text. Note the substantial differences among the phase responses.

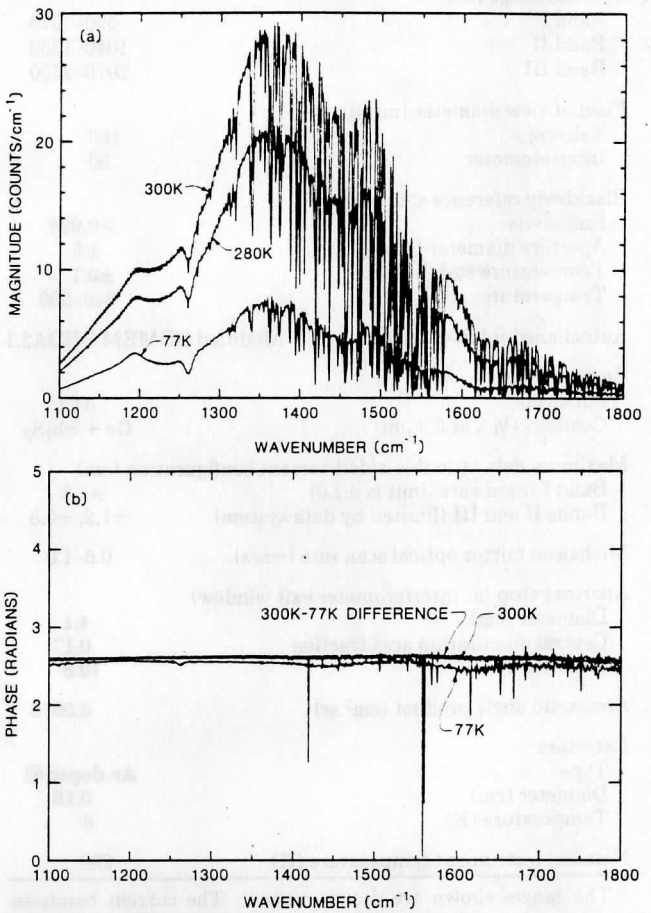

Fig. 3. Uncalibrated magnitude (a) and phase (b) spectra of blackbody sources for HIS spectral band II. The curves are labeled as in Fig. 2. Here also the magnitude spectra are shaped by a numerical filter and display channeling as discussed in the text. The very deep and numerous lines in the magnitude spectra are due to H_2O absorption. In contrast to band I, the phase spectra are very similar and quite linear.

linear phase contribution arising from an ambiguity in the sample offset from the zero path difference (ZPD) has also been removed.

The magnitude spectra have various features which need explanation. Because testing was conducted in air, the instrument transmittance is significantly affected by the 1–2 m of air in the path from the blackbodies to the detectors. (Of the total optical path between the blackbodies and the detector/Dewar assembly, only the interferometer itself is enclosed and backfilled with dry nitrogen to protect the beam splitter; at flight altitudes of 20 km, atmospheric absorption is insignificant.) Therefore, the magnitude spectrum for band I (600–1100 cm^{-1}) shows CO_2 absorption between 600 and 750 cm^{-1}, and band II (1100–1800 cm^{-1}) shows water vapor absorption beyond 1300 cm^{-1}. The absorption for the 668-cm^{-1} CO_2 line and for several H_2O lines is so strong in air that the signal is almost zero, and the phase is poorly defined. The general Gaussian shape of the magnitude spectra is caused by the numerical filtering which is performed in the instrument digital electronics. (A hardware convolution is performed for signal-to-noise preserving sample volume reduction by factors of 14, 8, and 8 in the three spectral bands.)

The sinusoidal components superimposed on the magnitude spectra are channeled spectra caused by the parallel surfaces of the arsenic-doped silicon detectors. (The band III detector has an antireflective coating, and the spectra do not display channeling.) The channeled spectra are very stable because the detectors, which are operated in a liquid He Dewar, have a very small coefficient of expansion and experience only small temperature variations. As will be shown in the next section, channeling does not affect calibrated spectra.

The phase spectra for bands I and II differ markedly. For band II the phases are nearly linear, the behavior expected with an ideal beam splitter having zero dispersion and with an electrical response having a pure time delay. Band I phases, on the other hand, show significant deviations from linearity and also vary as the source radiance is varied. The nonlinearity is optical, not electrical, in origin because the sign of the

deviations from linearity depends on delay scan direction. The phase spectra shown are for one scan direction. The corresponding phases for the other direction are approximately a mirror image about π rad.

B. Problem

It is probably not surprising, in light of the anomalous band I phases, that direct application of the normal calibration procedure (based on magnitude spectra) to the laboratory test data does not work uniformly well. The band I spectrum derived in this way is shown in Fig. 4. The spectrum is presented as a brightness temperature to make any errors stand out as a deviation from the measured blackbody temperature of 280.2 K. Errors of tens of degrees occur, and the similarity of the wavelength dependence of the errors to the nonlinearities of the phase is apparent. Figure 5 shows that the calibrated spectra for the HIS bands with nearly linear phase spectra are extremely accurate when calibrated in the same way. The region of large variance from 280.2 K beyond 1400 cm^{-1} for band II and centered near 2350 cm^{-1} for band III is caused by water vapor and CO_2 in the optical path and does not occur when the instrument is operated at flight altitude. Apparently, the normal calibration approach cannot handle measurements with phase anomalies like those of band I.

III. Solution

A. New Calibration Analysis

The band I phase spectra shown in Fig. 2(b) indicate that the phase becomes more nearly linear as the source radiance becomes larger. This behavior suggests that the total measured interferogram and the corresponding complex spectrum have two components; a normal phase component for radiance from the source and an anomalous phase component for radiance from the instrument itself. Of course, the radiance from the instrument can originate from many individual components with different phase characteristics, but they can be lumped together into one term with one phase.

The new calibration analysis is a generalization which properly accounts for a dual phase response, if it is present. It is really a minor modification of the procedure presented in Sec. II. The difference is that the complete complex spectra obtained from Fourier transforming the measured interferograms are used for calibration, not just the magnitudes. Let the complex uncalibrated spectrum be represented by

$$C'_\nu = \tilde{F}_\nu = r_\nu\{L_\nu + L^0_\nu \exp[i\phi^0(\nu)]\} \exp[i\phi(\nu)], \quad (7)$$

where ϕ^0 is the difference from the normal phase of the anomalous phase associated with the combined radiance from the many emitting components of the instrument. Then it is clear, under the same instrument stability assumptions on which the basic calibration approach depends, that the anomalous phase contribution can be eliminated along with the instrument radiance offset by differencing complex spectra from

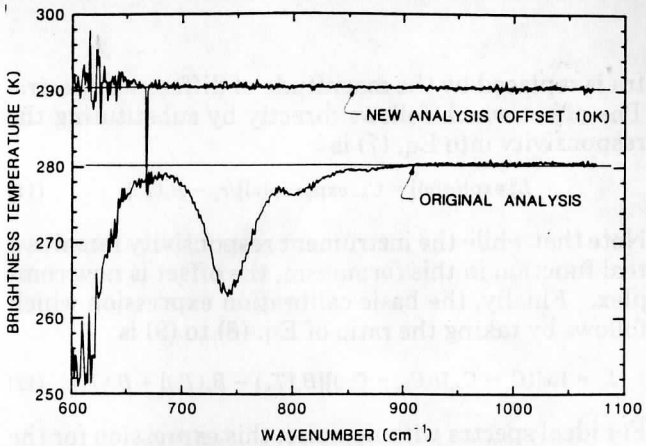

Fig. 4. Brightness temperature spectra for band I. The spectrum with the large deviations from the measured 280.2 K temperature of the blackbody source is derived from the original calibration analysis using magnitude spectra. The spectrum which accurately reproduces a constant brightness temperature is from the modified analysis presented here. The large variance between 600 and 650 cm^{-1} is caused by the low instrument transmittance in that region. Changes have since been made to improve the throughput in this region.

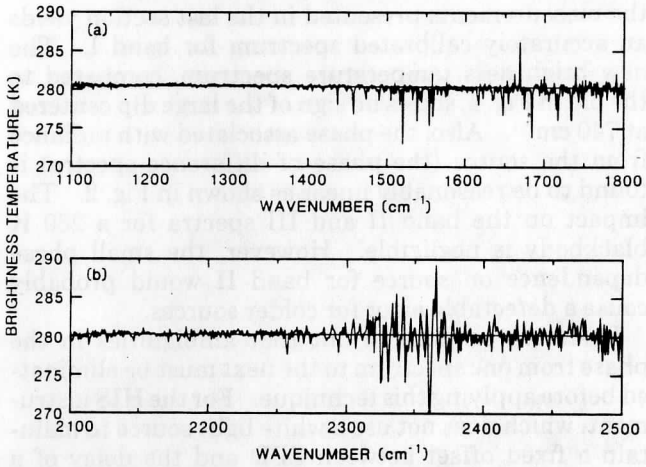

Fig. 5. Brightness temperature spectra for band II (a) and band III (b). The calibration for these bands is good and essentially identical for the standard and modified analyses. The larger variance beyond 1400 cm^{-1} for band II and centered at 2350 cm^{-1} for band III are due to H_2O and CO_2 in the path of the interferometer.

different sources. The difference spectra are identical to the difference spectra which would result if there were no anomalous phase contribution. The equations for the difference spectra from Eq. (7) are

$$C'_\nu - C'_{c\nu} = r_\nu[L_\nu - B_\nu(T_c)] \exp[i\phi(\nu)], \quad (8)$$

$$C'_{h\nu} - C'_{c\nu} = r_\nu[B_\nu(T_h) - B_\nu(T_c)] \exp[i\phi(\nu)]. \quad (9)$$

The new expression for the responsivity, which follows immediately from Eq. (9) by taking the magnitude of both sides, is

$$r_\nu = |C'_{h\nu} - C'_{c\nu}|/[B_\nu(T_h) - B_\nu(T_c)]. \quad (10)$$

Compared to Eq. (3), the difference of magnitude spec-

tra is replaced by the magnitude of difference spectra. The offset which follows directly by substituting the responsivity into Eq. (7) is

$$L_\nu^0 \exp[i\phi(\nu)] = C'_{h\nu} \exp[-i\phi(\nu)]/r_\nu - B_\nu(T_c). \quad (11)$$

Note that while the instrument responsivity remains a real function in this formalism, the offset is now complex. Finally, the basic calibration expression which follows by taking the ratio of Eq. (8) to (9) is

$$L_\nu = \mathrm{Re}[(C_\nu - C_{c\nu})/(C_{h\nu} - C_{c\nu})][B_\nu(T_h) - B_\nu(T_c)] + B_\nu(T_c). \quad (12)$$

For ideal spectra with no noise, this expression for the calibrated radiance would be real, since the phases of the ratioed difference spectra are the same. This cancellation of the phases avoids the square root of two noise amplification, which can be associated with taking the magnitude of spectra with nonzero phase. Because the phase of the ratio of difference spectra is zero to within the noise, the calibrated spectrum can equally well be defined in terms of the real part of the ratio (as shown) or in terms of the magnitude of the ratio.

This technique solves the problem. Application to the measurements presented in the last section yields an accurately calibrated spectrum for band I. The new brightness temperature spectrum, compared to the old in Fig. 4, shows no sign of the large dip centered at 740 cm^{-1}. Also, the phase associated with radiance from the source (the phase of difference spectra) is found to be reasonably linear as shown in Fig. 2. The impact on the band II and III spectra for a 280 K blackbody is negligible. However, the small phase dependence on source for band II would probably cause a detectable error for colder sources.

It should be pointed out that ambiguities in the phase from one spectrum to the next must be eliminated before applying this technique. For the HIS instrument, which does not use a white light source to maintain a fixed offset between ZPD and the delay of a numerically filtered point, a discrete ambiguity occurs. This translational ambiguity is linear in wavenumber and takes the form

$$\phi_k = \pi mk/MR, \quad (13)$$

where k is an integer, m is the spectral sample number, M is the number of points in the spectrum, and R is the numerical filter sample reduction factor. The ambiguity is removed by determining the k for each spectrum, which nearly eliminates the phase slope. Ambiguities of π rad, which occur in instruments with ambient temperature detectors, are not usually a consideration for the HIS application which uses LHe cooled detectors.

Also, note that if a white light source is used to control numerical filtering so that the same delays are measured on subsequent scans, the differencing to eliminate instrument background can be performed on the interferograms. Then anomalous phases would have no effect on spectra. Differencing interferograms is also the way to handle a potential dual phase problem, if one-sided OPD scanning is used.

B. Source of the Anomalous Phase Spectrum

It is of interest to explore the cause of the anomalous band I phase to assess the applicability of the new analysis technique to other FTIR applications. Also, it may be possible to relax constraints on interferometer optical design, since some apparent hardware problems can be eliminated by analysis.

Phase nonlinearities can of course occur from dispersion in beam splitter/compensator substrates, if their thicknesses are not well matched. This effect cannot explain the HIS data. The linearity of the phases for bands II and III suggests that the beam splitter/compensator matching is quite good. More important, dispersion from this origin does not give phase spectra which depend on the source.

To explain the HIS data, a mechanism is needed for which radiance from the instrument can yield a phase spectrum which is different from that for an external source. Apparently, the plane of wavefront division in the beam splitter depends on the source of the radiation. We have identified two mechanisms by which a source dependence might occur: (1) dependence of the beam splitter coating properties on the angle of incidence and (2) emission from the beam splitter coatings.

The first mechanism, angle dependence, has been ruled out as an important factor for the HIS configuration. A test was performed to measure off-axis radiation. It consisted of viewing a LN_2 source with the instrument in its normal configuration and with the field stop removed. The spectrum with the field stop removed is dominated by radiance from the Dewar window entering the interferometer exit window, not radiance from the field stop as in the normal configuration. The difference in the spectra for these two configurations is the spectrum of radiation from the field stop. The phase of the difference is essentially identical to that of radiance from an external source (Fig. 2), indicating no significant dependence on the angle of incidence.

The second possible mechanism, beam splitter coating emission, appears to be a likely candidate for explaining the anomalous phase. Beam splitter emission could lead to the effective wavefront division occurring at the point of emission with coherent radiation being emitted into both legs of the interferometer. Emission at a different depth in the beam splitter than normal wavefront division would create an anomalous phase.

There is evidence that the HIS beam splitter has absorption in the wavenumber region where phases are anomalous. Although the absorption of the beam splitter used for the measurements presented here has not been measured directly, transmittance measurements for other beam splitters of the same construction are available. Figure 6 shows the transmittance of one such beam splitter compared to a sinusoidal fit used to extrapolate the expected transmittance in the absence of absorption into the region of the narrow absorption feature centered at ~740 cm^{-1}. The minimum reflectance at 3000 cm^{-1} is consistent with the

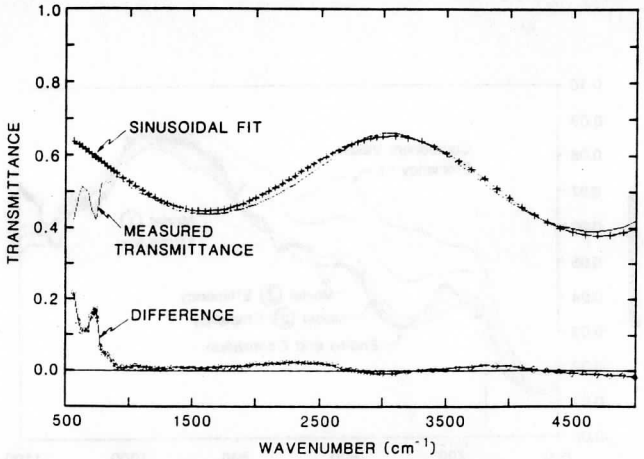

Fig. 6. Transmittance of a beam splitter of the same construction as the HIS instrument beam splitter. The absorption feature centered at ~740 cm^{-1} is responsible for the dual phase response of the instrument. The sinusoidal fit to the transmittance is used to approximate the reflectance for beam splitter emittance and efficiency calculations.

thickness of the beam splitter coatings, 0.25 wavelength at 3.3 μm of Ge and the same of Sb_2S_3. While germanium has a weak absorption feature centered near 740 cm^{-1}, the absorptance of up to 0.1 or 0.2 implied by these data is surprising, because the thickness of the coatings is not large enough for substantial bulk absorption. Maybe the indicated absorption is caused by a surface effect or contamination.

It is possible to obtain information on the beam splitter emittance and efficiency directly from measurements of the HIS instrument itself, if a model of the beam splitter is assumed. The two simple models illustrated in Fig. 7 have been used for this purpose. Rays illustrating the reflection process for an external source and the emission process are shown for both. Model 1 represents the beam splitter/compensator as a single plane with nonzero reflectance ρ and emittance ϵ. It is too simple to explain a phase anomaly, because there is a single surface for wavefront division due to both reflection and emission. Model 2 uses two plane surfaces, one which can reflect but not emit and one which can emit but not reflect. A beam splitter representable by this model would create an anomalous phase.

Emittances and efficiencies are determined from the ratio of the uncalibrated magnitude spectrum for emission from the beam splitter (referred to interferometer input) to that of a blackbody at the same temperature. The blackbody spectrum, free of emission contributions, is obtained in the normal manner by differencing the complex spectrum of an ambient temperature blackbody from the spectrum of a liquid nitrogen blackbody. The beam splitter spectrum is obtained by subtracting a scaled blackbody spectrum from the liquid nitrogen spectrum with the scale factor chosen to give approximately zero from 950 to 1100 cm^{-1} where absorption is expected to be small. The ratio defined in this way is equal to the ratio of the expressions for the emitted and reflected output given

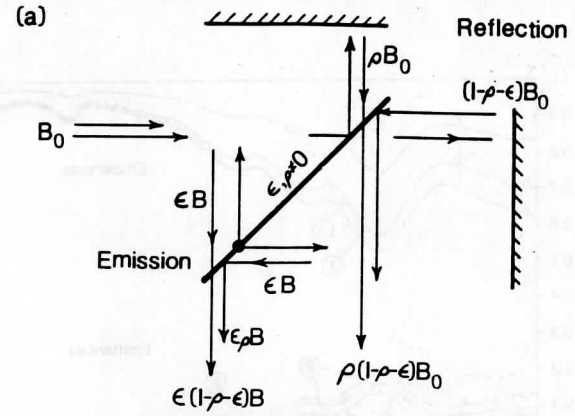

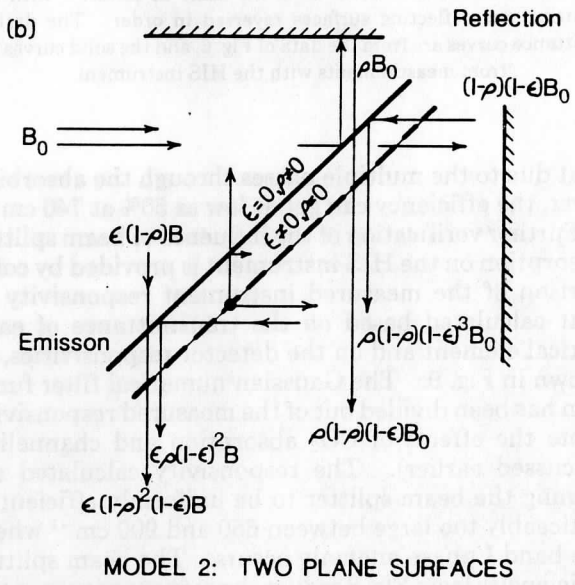

Fig. 7. Simplified beam splitter models for emittance and efficiency calculations. The expressions in terms of the emittance ϵ and reflectance ρ represent the amplitudes of the beam at various locations. The rays on the left represent the emission process, and those on the right represent the passage of an external beam.

in Fig. 7 (e.g., ratio = ϵ/ρ for model 1). Using the reflectivity from the sinusoidal fit of Fig. 6 [fit = $(1-\rho)$], the expression for the ratio can be solved for the emittance. The efficiency of the beam splitter is then given by the product of the complete beam splitter reflectivity and transmittance divided by the ideal output amplitude of 0.25 for a reflectance of 0.5 and no absorptance.

The emittances and efficiencies deduced from interferometer measurements using these models are shown in Fig. 8. The emittances estimates are in reasonable agreement with those obtained from the direct transmittance data of Fig. 6, giving further support for the conclusion that there is beam splitter emission acting approximately as modeled. Notice

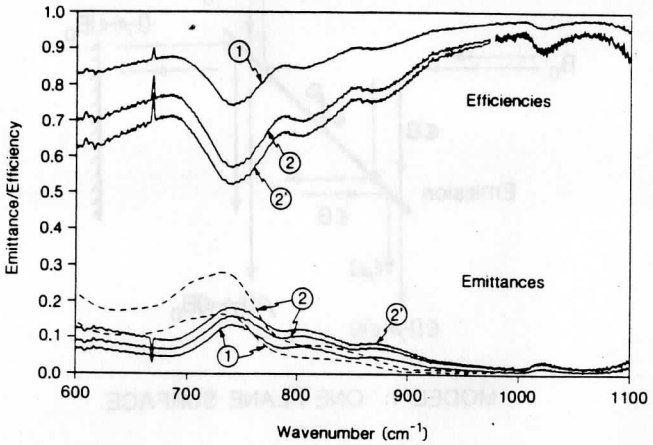

Fig. 8. Beam splitter emittance and efficiency estimates labeled by the model assumed. Model 2′ is the same as model 2 with the emitting and reflecting surfaces reversed in order. The dashed emittance curves are from the data of Fig. 6, and the solid curves are from measurements with the HIS instrument.

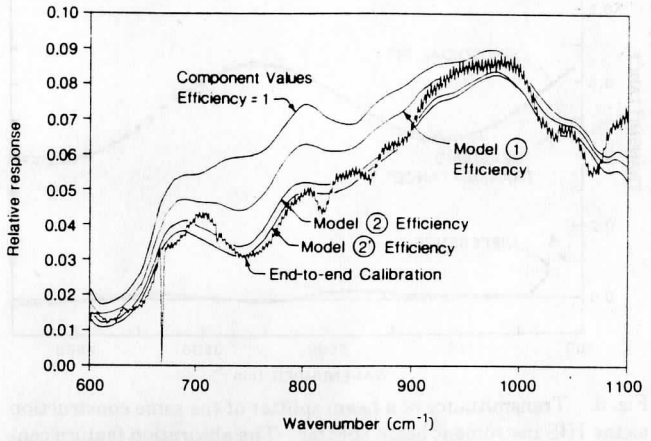

Fig. 9. Comparison of instrument responsivity calculated from optical component transmittances and detector responsivity to the end-to-end responsivity from calibration measurements. The beam splitter efficiencies used in the calculated responsivities are those deduced from measurements with the HIS interferometer itself. The calculations using model 2 seem to account properly for actual beam splitter efficiencies.

that due to the multiple passes through the absorbing layer, the efficiency can get as low as 50% at 740 cm^{-1}.

Further verification of the influence of beam splitter absorption on the HIS instrument is provided by comparison of the measured instrument responsivity to that calculated based on the transmittance of each optical element and on the detector responsivities, as shown in Fig. 9. The Gaussian numerical filter function has been divided out of the measured responsivity (note the effects of CO_2 absorption and channeling discussed earlier). The responsivity calculated assuming the beam splitter to be uniformly efficient is noticeably too large between 650 and 900 cm^{-1} where the band I phase anomaly occurs. The beam splitter efficiencies from Fig. 8 reduce the responsivity over the correct wavenumber region, with the model 2 calculation giving very good agreement with the measured responsivity.

Both the deduced emittances and the efficiencies give a strong case for the emission explanation of anomalous phases. However, a piece of puzzle that does not fit very well is the size of the phase anomalies. The optical thickness ($x = \delta\phi/2\pi\nu$) corresponding to the observed phase anomalies ($\delta\phi$) at 740 cm^{-1} is 3.9 μm. Model 2 suggests that, if the absorption is in the coatings, the additional optical path difference should be <1.9 μm, the optical thickness of the combined beam splitter coatings divided by the cosine of the 30° angle of incidence. This peculiarity and the mechanism for the absorption are remaining mysteries.

IV. Implications and Summary

It is not known whether the problem identified here is common or rare in other FTIR applications. The errors resulting from this problem could possibly be small enough to go unnoticed but might be significant when evaluating detailed performance. Comparing the phase spectra for a cold and a warm source is a simple test for diagnosing the problem.

The new calibration analysis technique has been discussed here in the context of the HIS application, involving absolute radiance measurements. It may also be important for applications in which the transmittance or reflectance of a sample is measured. As pointed out by Tanner and McCall,[13] emission from the samples or the surroundings can create significant errors for these types of measurement. However, the radiance contribution from the background can be eliminated, if the spectra for two different reference sources are differenced. By determining the difference spectra using complete complex spectra as described in the last section, any anomalous phase contributions of radiance from the interferometer will also be eliminated.

There are some aspects of interferometer design that may be influenced by the analysis approach presented here and by knowledge that beam splitter emission can modify the phase response. First, the constraints on beam splitter coating materials can probably be relaxed to include materials with some absorption. Second, interferometer designs may be able to rely on a better capability to handle errors associated with the phase. It is conceivable that having a well-behaved phase is not so important when a proper calibration is performed with double-sided scanning.

In summary, the phase response of one spectral band of the HIS FTIR instrument appears to vary with the source radiance, becoming more linear the higher the radiance contribution from the source. This dependence creates substantial radiance errors when magnitude spectra are used to perform a two-point calibration using blackbody reference sources. The errors are eliminated, yielding good calibration results, when a minor modification to this technique is applied. The new technique explicitly accounts for the possibility that a dual phase response can occur. That is, the phase response for radiance from the instrument can

differ from that for radiance from a source. The origin of the different phase response for radiance from the HIS instrument is identified as emission from the beam splitter.

The authors thank the members of the instrument team at the Space Science and Engineering Center, BOMEM, Inc., the Santa Barbara Research Center, and the University of Denver, whose care in fabricating and aligning the HIS instrument made accurate radiometric calibration realizable. Thanks also to Frank Murcray for many helpful discussions. The HIS program is jointly funded by NOAA contract NA-84-DGC-00095 and NASA contract NAS5-27608.

References

1. W. L. Smith, H. E. Revercomb, H. B. Howell, and H. M. Woolf, "Recent Advances in Satellite Remote Sounding," *International Radiation Symposium '84: Current Problems in Atmospheric Radiation*, G. Fiocco, Ed. (A. Deepak, Hampton, VA, 1984), p. 388.
2. W. L. Smith, H. E. Revercomb, H. B. Howell, and H. M. Woolf, "HIS—A Satellite Instrument to Observe Temperature and Moisture Profiles with High Vertical Resolution," in *Fifth Conference on Atmospheric Radiation* (American Meteorological Society, Boston, 1983).
3. R. A. Hanel, B. Schlachman, F. D. Clark, C. H. Prokesh, J. B. Taylor, W. M. Wilson, and L. Chaney, "The Nimbus III Michelson Interferometer," Appl. Opt. **9**, 1767 (1970).
4. R. A. Hanel, B. Schlachman, D. Rodgers, and D. Vanous, "Nimbus 4 Michelson Interferometer," Appl. Opt. **10**, 1376 (1971).
5. D. Oertel *et al.*, "Infrared Spectrometry of Venus from Venera-15 and Venera-16," Adv. Space Res. **5**, 25 (1985).
6. R. A. Hanel *et al.*, "Mariner 9 Michelson Interferometer," Appl. Opt. **11**, 2625 (1972).
7. R. A. Hanel *et al.*, "Infrared Spectrometer for Voyager," Appl. Opt. **19**, 1391 (1980).
8. J. W. Brault, "Fourier Transform Spectroscopy," *High Resolution Astronomy*, Proceedings, Fifteenth Advanced Course in Astronomy and Astrophysics, Saas-Fee, M. Huber, A. Benz, and M. Mayor, Eds. (1985).
9. "A Design Feasibility Study for the High-Resolution Interferometer Sounder (HIS)," Santa Barbara Center Final Report for contract UAA 871R55 5 (10 July 1981, updated 19 July 1982, updated 15 Feb. 1983).
10. W. L. Smith, H. E. Revercomb, H. M. Woolf, H. B. Howell, D. D. LaPorte, and K. Kageyama, "Improved Geostationary Satellite Soundings for the Mesoscale Weather Analysis/Forecast Operations," in *Proceedings, Symposium on Mesoscale Analysis and Forecasting*, Vancouver, Canada, 17–19 Aug. 1987, ESA SP-282 (1987).
11. H. E. Revercomb, D. D. LaPorte, W. L. Smith, H. Buijs, D. G. Murcray, F. J. Murcray, and L. A. Sromovsky, "High-Altitude Aircraft Measurements of Upwelling IR Radiance: Prelude to FTIR from Geosynchronous Satellite," Mikrochim. Acta in press, 000 (Springer-Verlag, Wien, 1987).
12. D. D. LaPorte and R. Howitt, "Ambient Temperature Absolute Radiometry using Fourier Transform Spectrometers," Proc. Soc. Photo-Opt. Instrum. Eng. **364** (1982).
13. D. B. Tanner and R. P. McCall, "Source of a Problem with Fourier Transform Spectroscopy," Appl. Opt. **23**, 2363 (1984).